

Inorg Chem. Author manuscript; available in PMC 2010 July 23.

Published in final edited form as:

Inorg Chem. 2009 August 3; 48(15): 7280–7293. doi:10.1021/ic900778k.

Imidazole-Containing (N₃S)-Ni^{II} Complexes Relating to Nickel Containing Biomolecules

Roxanne M. Jenkins, Michael L. Singleton, Elky Almaraz, Joseph H. Reibenspies, and Marcetta Y. Darensbourg*

Department of Chemistry, Texas A&M University, College Station, Texas 77843

Abstract

Dimeric $(N_2S)Ni$ complexes and the monomeric N_2S_2 bismercaptodiazacycloheptane nickel complex, (bme-dach)Ni, serve as precursors to two N_2 -, N'-/S- complexes where N_2 -diazacycloheptane, N'-imidazole and S=thiolate. As rare examples of nickel complexes containing a mixed thiolate/imidazole ligand set, these complexes are characterized by X-ray diffraction, UV/vis, and variable temperature 1H NMR spectroscopies, and electrochemistry. Density functional theory computations relate the orientation of the imidazole with respect to the $N_2N'SNi$ square plane to the VT NMR observed fluxionality and activation parameters. The superoxide dismutase activity of the imidazole complexes was investigated by the nitroblue tetrazolium assay.

Introduction

The reactivity of tetradentate N_2S_2 ligands containing nucleophilic S-sites in transition metal thiolate complexes has been extensively explored. In our laboratory, metalation, S-oxygenations, and alkylations have been used to establish reactivity of the neutral (bmedaco)Ni(II) complex, bme-daco=bismercaptoethanediazacyclooctane, the neutral (bmedach)Ni(II) complex, bme-dach=bismercaptoethanediazacycloheptane, as well as the anionic $[Ni(II)(ema)]^{2-}$ complex, ema=N,N'-ethylenebis-2-mercaptoacetamide. $^{1-3}$ Coupled with S-thiolates, such amine, amide, or mixed amine/amide N-donor ligand environments have been proposed by us and others to serve as biomimetics of metalloenzyme active sites. 4

The preparation of histidine/cysteine mixed donor binding sites was first demonstrated in small peptidic complexes by Suguri et al., as models of blue copper proteins. Nickel complexes of $-X_{aa}-X_{aa}$ -His- tripeptide motifs have been studied in detail for their ability to influence DNA damage and cross-linking through oxidative processes. To explore the potential oxidative chemistry of cysteine thiolates, Burrows and co-workers synthesized the cysteine variants, $-X_{aa}$ -Cys-His- and -Cys- X_{aa} -His-, as possible metal binding sequences. Na twas found that aerobic oxidation of such complexes with cysteine in the second position, $-X_{aa}$ -Cys-His-, led to the rapid formation of disulfide dimers. In this case, other oxidized products such as metallosulfoxides or metallosulfones were not reported. The dimeric

Note Added in Proof: During the review of this manuscript, Harrop and co-workers reported a similar (N₂S)₂Ni₂ dimer cleavage reaction as a versatile route to NiSOD biomimetics. (Gale, E.M.; Patra, A. K.; Harrop, T. C. *Inorg. Chem.* 2009, ASAP.)

^{*}To whom correspondence should be addressed. marcetta@mail.chem.tamu.edu.

Supporting Information Available: Summary of crystallographic data for complexes 1–5, packing diagram of complex 4, electrochemical data, experimental and optimized parameters for complexes 3 and 4, DFT calculated energies and compositions of frontier molecular orbitals of complexes 3 and 4, DFT predicted ¹H NMR predictions for the imidazole protons of complex 3, ESI-MS data for oxygenated derivatives of complex 3, and full citation for the Gaussian 03 program (ref ³⁰). This material is available free of charge via the Internet at http://pubs.acs.org

disulfide-bridged complex was found to have no further reactivity with oxygen even though $\mathrm{Ni^{II}}$ peptides with carboxylate termini are known to spontaneously decarboxylate in air. In contrast, the $\mathrm{Ni^{II}}$ derivative of N-terminal -Cys- X_{aa} -His- resulted in the formation of a cysteine sulfinic acid under aerobic conditions. Whether the plethora of possibilities of oxidative products complicate or play fundamental roles in the chemistry underlying biological action is not well understood.

Recently, the molecular structures of NikR and NiSOD revealed nickel(II) sites which contain both N-histidine and S-cysteine ligands, Figure 1.9–11 The transcription factor NikR serves as a cytoplasmic nickel sensor in *Escherichia coli* and the human gastric pathogen *Helicobacter pylori*. It is responsible for stopping the production of the nickel importer, nikABCDE, when intracellular levels of nickel are sufficient. NikR is a homotetramer protein which incorporates one Ni^{II} ion per subunit in square-planar coordination consisting of the side chains of two histidine and one cysteine residue from one NikR monomer, and a side chain histidine from an adjacent monomer. Biomimetic studies of this nickel(II) binding site have not been reported.

The Ni^{II/III} redox couple is used in NiSOD catalysis for the disproportionation reaction of superoxide to O_2 and H_2O_2 . ¹⁴ The reduced form of the active site of NiSOD features a square planar geometry about Ni^{II} consisting of the N-terminus amine nitrogen, a carboxyamido N atom, two cysteine thiolates, and possibly a fifth donor ligand from an axial histidine N atom. The molecular structure of the oxidized form reveals axial imidazole coordination to the Ni metal center, Figure 1.9,10

In recent years, considerable work has been targeted toward understanding how the NiSOD enzyme avoids S-oxygenation and/or S-oxidation in the presence of the products of SOD, O_2 , and H_2O_2 . Computational investigations have concluded that the presence of one or two amide donors within the N_2S_2 core promotes metal-based chemistry. ¹⁵ There has been significant progress in the preparation of synthetic mimics of the NiSOD active site. In particular, a mixed amine/amide donor set in the N_2S_2 core has resulted in a Ni^{II} complex with a ligand environment similar to the reduced state of the native enzyme, and this NiSOD mimic demonstrated enhanced stability toward oxygenation. ¹⁶ As cis dithiolate sulfurs in Ni^{II} complexes have been shown to form stable S-oxygenates in both neutral and dianionic N_2S_2Ni complexes, we have suggested that kinetic control accounts for the lack of S-oxygenates in the enzyme active site of NiSOD. ³

Jensen and co-workers have utilized "scorpionate" ligands to mimic the nitrogen donors and dithiocarbamates and organoxanthate to mimic the dithiolate ligands of the NiSOD binding motif to obtain a five-coordinate $N_3S_2Ni(II)$ complex. ¹⁷ Although synthetic N_2S_2Ni complexes as NiSOD active site mimics have similar spectroscopic features as the native enzyme and quasi-reversible redox couples in the range of SOD dismutation, Shearer and Zhao's model complexes did not produce catalytic activity for superoxide dismutation. ^{16b} Neither did Jensen et al. report SOD activity. ¹⁷ Nevertheless, nickel peptide-based models mimicking the amino acid nickel-hook sequence found in the native NiSOD enzyme have been more successful, demonstrating compatible electrochemistry as well as SOD activity. ¹⁸ Studies by Shearer and co-workers also suggest that the His imidazole remains ligated throughout SOD catalysis, and this is supported by computational studies of Siegbahn et al. ^{19,20}

Very little is known about how the electronic structure of Ni^{II} complexes containing both imidazole and thiolate ligation responds to oxidation and how this might affect SOD catalysis and response to the H_2O_2/O_2 products. To address this, two synthetic models containing a continuous and discontinuous $N_2N'S$ donor set have been prepared. For this

study, a dimeric dithiolate bridged Ni^{II} dication and the readily accessed (bme-dach)Ni(II) were used as the precursors to mixed imidazole/thiolate complexes. The work herein reports the synthesis, characterization, and molecular structures of both continuous tetradentate ($N_2N'S$) and discontinuous (N_2S-N') synthetic models incorporating simple imidazoles as His mimics. Variable temperature 1H NMR studies in correlation with density functional theory (DFT) calculations have been carried out to further investigate the orientation of the imidazole ligand. The physical properties of the derivatives and precursors and preliminary studies of SOD activity are described.

Experimental Section

General Procedures

Air sensitive materials were handled using standard Schlenk techniques or in an Ar-filled glovebox. Solvents were purified and degassed via a Bruker solvent system. All reagents were purchased from Aldrich Chem. Co. and used as received unless noted. Isobutylene sulfide,²¹ (bme-dach)Ni,^{2a} and 4-(chloromethyl)-5-methyl-1*H*-imidazole hydrochloride²² were prepared according to published procedures.

Physical Measurements

UV–vis spectra were recorded on a Hewlett-Packard 8453 diode array spectrometer and a Cary1E spectrophotometer using quartz cells (1.00 cm path length). Mass spectrometry (ESI-MS) was performed by the Laboratory for Biological Mass Spectrometry at Texas A&M University. ¹H NMR spectra were obtained on a Mercury-300 FT-NMR spectrometer and variable temperature ¹H NMR spectra were recorded on an Inova500 spectrometer operating at 500 MHz. CD₃OD was used as solvent, and all resonances were referenced to MeOH (CH₃: 3.31 ppm) at all temperatures. Conductance measurements of millimolar concentrations of analyte were made using an Orion 160 conductivity meter. Elemental analyses were performed by Atlantic Microlab, Inc., Norcross, Georgia or by Canadian Microanalytical Services, Ltd., Delta, British Columbia, Canada.

Electrochemistry

Cyclic, square wave and differential pulse voltammograms were recorded on a BAS100W potentiostat under an Ar atmosphere using a three electrode cell, which consisted of a glassy carbon disk (0.071 cm²) working electrode, a coiled platinum wire counter electrode, and $Ag^0/AgNO_3$ reference electrode. Samples were measured in DMF with Bu₄NBF₄ (0.1 M) as the supporting electrolyte and at potential scan rates of 200 mV/s. Ferrocene was added as an internal standard, and all potentials are reported relative to $Ag^0/AgNO_3$ electrode using Cp_2Fe/Cp_2Fe^+ as reference ($E_{1/2}$ =0.00 V vs $Ag^0/AgNO_3$ in DMF). The reversibility of the observed redox couples is based on the internal reference (Cp_2Fe/Cp_2Fe^+). The peak-to-peak separations ($Ep_a - Ep_c$) for the complexes studied herein are larger than the 59 mV expected for a reversible one-electron process, but comparable with $Ep_a - Ep_c$ for the Cp_2Fe/Cp_2Fe^+ couple under the same conditions. The ratios of the anodic and cathodic peak currents were close to unity for the assigned reversible systems. Bulk electrolysis was carried out using a BAS 100A potentiostat and BAS bulk electrolysis cell containing 30 mL of DMF which was 1.0mMin 3 and 0.1Min Bu₄NBF₄ under an argon atmosphere. The working electrode of the BAS bulk electrolysis cell was comprised of reticulated vitreous carbon.

X-ray Crystal Structure Analyses

X-ray data were obtained on a Bruker SMART 1000 CCD based diffractometer (Texas A&M University) operating at 110 K.²³ The X-ray radiation was generated from a Mo sealed X-ray tube ($K\alpha = 0.70173 \text{ Å}$). Structures were solved using SHELXTL;²⁴ absorption correction, SADABS; structure solution, SHELXS-97 (Sheldrick);²⁵ structure refinement,

SHELXL-97 (Sheldrick);²⁶ and molecular graphics and preparation of material for publication, SHELXTLPLUS, version 5.1 or later (Bruker). Experimental conditions and crystallographic data are listed in the Supporting Information.

Computational Details

Initial geometries were derived from X-ray structures or deductions based on conformations resulting from fluxional processes in the molecules. In both cases, the conformational space near each of the starting geometries was sampled through simulated annealing calculations in the gas phase using the Cerius² software package.²⁷ The simulated annealing calculations were carried out using the Open Force Field (OFF) module with the Universal Force Field (UFF) for 15 annealing cycles, over a temperature range of 300–5000 K, with $\Delta T = 50$ K. The compounds were minimized after each annealing cycle resulting in 15 conformations. The initial geometry and low energy conformations were then optimized using DFT, with the Becke three-parameter exchange functional (B3)²⁸ and the Lee–Yang–Parr correlation functional (LYP) (B3LYP).²⁹

All theoretical calculations, including optimization, frequency, and NMR, were performed with the Gaussian 03 suite programs. The Stuttgart–Dresden (SDD) effective core potential and valence basis set were used for nickel. For sulfur, the effective core potential and basis set of Hay and Wadt were used with inclusion of a modified polarization function developed by Hŏllworth et al. For nitrogen, the correlation-consistent polarized valence double- ζ basis set of Dunning and co-workers (cc-pVDZ) was used. All carbon and hydrogen atoms were represented using the split valence double- ζ basis set of Pople and co-workers with polarization functions on heavy and light atoms (6-31 g(d',p')).

Synthesis of 1-(2-Mercaptoethyl)-methyl-1,4-diazacycloheptane, me-mdach

Similar to the preparation of the N_2S_2 ligand Hmmp-dach, 36 under N_2 , N-methylhomopiperazine (5 mL, 0.0402 mmol) was dissolved in 50 mL of dry MeCN. With stirring, the solution was heated to 50 °C under N_2 , and an excess of ethylene sulfide (8 mL, 0.134 mmol) was added slowly forming a white solid and a light yellow solution. Heating was continued for 20 h after which the solution was anaerobically filtered through Celite, giving a light yellow solution. The solvent was removed in vacuo resulting in a yellow oil, 3.33 g, 48% yield. $C_8H_{18}N_2S$ (MW=174 g/mol) ^+ESI -MS: m/z=175 [M+H] $^+$. 1H NMR (CDCl₃): δ (ppm)=1.83 (q, 2.0 H), 2.38 (s, 2.9 H), 2.64 (m, 4.2 H), 2.77 (m, 5.2 H), 2.86 (m, 2.6 H).

1-(2-Mercapto-2-methylpropyl)-methyl-1,4-diazacycloheptane, mmp-mdach

1-(2-Mercapto-2-methylpropyl)-methyl-1,4-diazacycloheptane, mmp-mdach, was prepared in a similar manner to the above using isobutylene sulfide. A light yellow oil was isolated in 31% yield. $C_{10}H_{22}N_2S$ (MW=202 g/mol) ⁺ESI-MS: m/z=203 [M+H]⁺.

Synthesis of [[1-(2-Mercaptoethyl)-methyl-1,4-diazacycloheptane] nickel(II)] Tetrafluoroborate, [(me-mdach)Ni]₂(BF₄)₂, Complex 1

Under N_2 , me-mdach (0.56 g, 3.22 mmol) was dissolved in 20 mL of dry MeOH. A solution of NaOMe (0.17 g, 3.17 mmol) in 10 mL of dry MeOH was added via cannula, and the mixture was stirred at room temperature (RT) for 1 h. A solution of Ni(BF₄)₂ · 6 H₂O (0.75 g, 3.23 mmol) in 25 mL of MeOH was added dropwise via cannula producing a red solution. After stirring at RT for 4 h the solvent volume was reduced to about 5 mL. Addition of 25 mL of MeCN resulted in the precipitation of NaBF₄ salts which were separated from the product by filtration in air. The solvent of the filtrate was removed in vacuo resulting in a tacky maroon residue. The residue was dissolved in a minimum of MeOH, and a maroon

solid was obtained on addition of diethyl ether. Alumina column chromatography was used to purify the crude product using MeCN as the eluent until a light yellow band was removed, followed by an elution mixture of MeOH/MeCN (1:25), which yielded a maroon band of pure [(me-mdach)Ni₂](BF₄)₂ (0.38 g, 37%). X-ray quality crystals were obtained by Et₂O diffusion into a MeCN solution at 5 °C. Elemental anal. Calcd (found) for Ni₂C₁₆H₃₄N₄S₂B₂F₈ (MW=638 g/mol): C, 30.14 (30.40); N, 8.78 (8.65); H, 5.37 (5.25). Absorption spectrum (MeOH): λ_{max} (ϵ , M⁻¹ cm⁻¹) 524 (817), 452 (775), 354 (2503), 305 (13075), 252 (13675), 229 (21330) nm. ⁺ESI-MS (MeCN): m/z=549 [(me-mdach)₂Ni₂)]BF₄⁺; 231 [(me-mdach)₂Ni₂]²⁺. Molar conductance at 23 °C: 299 S cm² mol⁻¹ (MeCN); 310 S cm² mol⁻¹ (H₂O).

Chloro-[1-(2-Mercaptoethyl)-methyl-1,4-diazacycloheptane] nickel(II), [(me-mdach)-NiCl]₂, Complex 2

Chloro-[1-(2-Mercaptoethyl)-methyl-1,4-diazacycloheptane]nickel(II), [(me-mdach)-NiCl]₂, complex **2**, was prepared and purified in a similar manner using NiCl₂ · 6H₂O as the metal source. The complex was purified by alumina column chromatography yielding pure [(me-mdach)NiCl]₂ as a reddish brown solid (31% yield). X-ray quality crystals were obtained by Et₂O diffusion into an MeCN solution at 5 °C. Elemental anal. Calcd (found) for Ni₂C₁₆H₃₄N₄S₂Cl₂ (MW=535 g/mol): C, 36.0 (37.0); N, 10.5 (10.2); H, 6.41 (6.76). Absorption spectrum (MeOH): λ_{max} (ε , M⁻¹ cm⁻¹) 527 (967), 490 (sh), 350 (3307), 307 (7816), 247 (17126), 211 (18002) nm. +ESI-MS: m/z = 497 [(me-mdach)₂-Ni₂Cl]⁺; 231 [(me-mdach)₂Ni₂]²⁺. Molar conductance at 23 °C: 124 S cm² mol⁻¹ (MeCN); 303 S cm² mol⁻¹ (H₂O).

$\label{lem:chloro-propyl} Chloro-[1-(2-Mercapto-2-methylpropyl)-methyl-1, 4-diazacycloheptane]\ nickel(II),\ [(mmp-mdach)NiCl]_2,\ Complex\ 2-Me_2$

Chloro-[1-(2-Mercapto-2-methylpropyl)-methyl-1,4-diazacycloheptane] nickel(II), [(mmp-mdach)NiCl]₂, complex **2**-Me₂, was obtained via the above method by using the mmp-mdach ligand. Absorption spectrum (MeOH): λ_{max} (ϵ , M⁻¹ cm⁻¹) 532 (904), 426 (988), 326 (6120), 283 (11940), 244 (21300), 205 (24580) nm. ⁺ESI-MS mass spectral analysis for Ni₂C₂₀H₄₂N₄S₂Cl₂ (MW= 591 g/mol): m/z = 553 [(mmp-mdach)₂Ni₂Cl]⁺; 259 [(mmp-mdach) Ni₂]²⁺. Molar conductance at 23 °C: 104 S cm² mol⁻¹ (MeCN); 299 S cm² mol⁻¹ (H₂O).

Synthesis of [1-(2-Mercapto-2-methylpropyl)-methyl-1,4-diazacycloheptane] nickel(II) Imidazole Chloride [(mmp-mdach)-Ni(Im)]Cl, Complex 3

After degassing and under N_2 , complex **2**, [(mmp-mdach)NiCl]₂, (0.102 g, 0.173 mmol) and imidazole (0.035 g, 0.514 mmol) were dissolved in 30 mL of dry MeOH, which immediately produced an orange solution. After stirring overnight, the solution volume was reduced to a minimum under vacuum, and Et_2O was added to precipitate the product. The ether was decanted, and the product was washed 2×25 mL of Et_2O to remove excess imidazole. Pure product was isolated as an orange solid (0.092 g, 71% yield). X-ray quality crystals were obtained by Et_2O diffusion into a MeOH solution at -30 °C. $NiC_{13}H_{25}N_4SCl$ Elemental anal. Calcd (found) for $NiC_{13}H_{25}-N_4SCl \cdot H_2O$ (MW = 382 g/mol): C, 40.92 (40.88); N, 14.68 (14.45); H, 7.13 (7.07). Absorption spectrum (MeOH): λ_{max} (ϵ , M^{-1} cm⁻¹) 467 (501), 340 (sh), 288 (10767), 211 (21461) nm. +ESI-MS (MeOH): m/z = 327 [(mmp-mdach)Ni(Im)]+. Molar conductance at 23 °C: 89 S cm² mol⁻¹ (MeOH); 156 S cm² mol⁻¹ (H₂O).

Synthesis of [1-(5-methyl-1*H*-imidazol-4-yl)methylthio)ethyl-4-mercaptoethyl-1,4-diazacycloheptane]nickel(II) Chloride [Ni-1'(CH₂-mlm)]Cl, Complex 4

A 100 mL Schlenk flask was charged with (bme-dach)Ni (0.100 g, 0.361 mmol). The solid was degassed and suspended in 25 mL of MeCN. A suspension of 4-(chloromethyl)-5-methyl-1H-imidazole hydrochloride (0.060 g, 0.361 mmol) in 25 mL of MeCN was transferred via cannula. As the reaction proceeded, the solids were drawn into solution followed by formation of a light pink precipitate. The mixture was stirred overnight. Filtration yielded a pink solid which was washed 3 × 75 mL of MeCN, dissolved in a minimum of MeOH, and recrystallized with Et₂O. The solid was washed 2 × 25 mL of Et₂O (45 mg, 31%). X-ray quality crystals were obtained by Et₂O diffusion into a MeOH solution. Elemental anal. Calcd (found) for NiC₁₄H₂₅N₄S₂Cl · H₂O (MW=426 g/mol): C, 39.50 (40.07); N, 13.16 (13.23); H, 6.39 (6.44). Absorption spectrum (MeOH): λ_{max} (ε , M^{-1} cm⁻¹) 469 (235), 288 (6052), 211 (16983) nm. +ESI-MS: m/z=371 [Ni-1'(CH2-mIm]+. Molar conductance at 23 °C: 103 S cm² mol⁻¹ (MeOH); 164 S cm² mol⁻¹ (H₂O).

Synthesis of [1,4-Bis(3-methylimidazol-4-ylmethyl)-1,4-diazacycloheptane nickel(II)] Tetrafloroborate, [(bmlme-dach)Ni]-(BF₄)₂, Complex 5

Synthesis, purification, and characterization of 1,4-bis(3-methylimidazol-4-ylmethyl)-1,4-diazacycloheptane penta-hydrochloride hydrate (L-5HCl \cdot H₂O) was executed following the procedure published by Bu et al. with 4-(chloromethyl)-5-methyl-1*H*-imidazole hydrochloride used in the place of 4-(chloromethyl)-1*H*-imidazole hydrochloride. A solution of Ni(BF₄)₂ \cdot 6 H₂O (1.328 g, 3.903 mmol) in 10 mL of MeOH was added dropwise to a stirring solution of L-5HCl \cdot H₂O (1.100 g, 3.814 mmol) in 15 mL of MeOH, resulting in immediate precipitation of yellow solid. The reaction mixture was stirred overnight at 22 °C under an N₂ blanket. The ensuing green solution and yellow solid were separated via filtration, and the solid was washed with Et₂O and dried in vacuo to yield 0.757 g (1.45 mmol, 38%). X-ray quality crystals were obtained by slow evaporation from a methanol solution. Elem. Anal. Calcd. (found) for NiC₁₅H₂₄N₆B₂F₈ (MW=521 g/mol): C, 34.60 (34.07); H, 4.65 (4.70); N, 16.14 (15.62). Absorption spectrum (MeOH): λ_{max} (ε , M⁻¹ cm⁻¹): 449(29), 280 (sh), 233 (2232) nm. ⁺ESI-MS in MeOH: [M]²⁺ m/z=173 [(bmImedach)Ni]²⁺. Molar conductance at 23 °C: 198 S cm² mol⁻¹ (MeOH); 223 S cm² mol⁻¹ (H₂O).

Results and Discussion

Synthesis and Structure of N_2S Bridged Thiolate Dimers: [(me-mdach)Ni]₂(BF₄)₂, 1, and [(me-mdach)NiCl]₂, 2

There are many examples of N_2S_2Ni complexes in μ_2S_2 -bridged dimers which demonstrate the diverse structural arrangements encountered by μ -S-thiolate bridging. Scheme 1 outlines the synthetic protocol for the N_2S thiolate bridged dimeric complexes 1 and 2 explored herein. Both are isolated as hygroscopic, air stable solids. Complex 1 is a deep maroon solid that is very soluble in MeCN and H_2O and moderately soluble in MeOH. Complex 2 is isolated as a reddish-brown powder and is very soluble in MeOH and H_2O and moderately soluble in MeCN. The molecular structures of 1 and 2 are shown in Figure 2 and a selection of metric data is given in Table 1. The dimeric form of complex 1 involves edged-bridged square planes with symmetry imposed disorder relating to the S to N linkers. The NiN_2S_2 unit is almost perfectly square planar with average standard deviation from the NiN_2S_2 plane of 0.0038 Å. The "hinge" angle in this butterfly type complex, that is, the dihedral angle between the two N_2S_2 best planes, is 116.7° ; the $Ni \cdots Ni$ distance is 2.837 Å. A similar dimer with gem dimethyl groups on the carbon α to the bridging sulfurs has a greater hinge angle of 135.7° and a $Ni \cdots Ni$ distance of 3.034 Å. These distances are

compatible with other complexes containing $(\mu_2\text{-SR})_2$ bridged Ni₂S₂ rhombs.³⁸ The closest BF₄⁻ counterion in **1** has an F··· Ni distance of 5.031Å.

In contrast to the μ -SR bridged square planar NiN₂S-(μ -S) of **1**, the solid state structure of **2** finds a penta-coordinate Ni^{II} in pseudotrigonal bipyramidal, N₂S(μ -S) Cl coordination (Figure 2). The equatorial plane in each tbp is comprised of one N-donor atom of the tridentate N₂S ligand, a chloro ligand, and a sulfur atom from the adjacent (N₂S)Ni moiety resulting in an Ni₂S₂ diamond core. The S-donor atom and the trans N-donor atom of the tridentate N₂S ligand make up the axial sites. The Ni–S_{axial} bond distance of **2** is slightly longer than Ni–S_{equatorial}. As expected, the average Ni–N and Ni–S distances are longer in the penta-coordinate chloride derivative **2** than in **1**, and an increase in the Ni · · · Ni distance, from 2.837 Å in complex **1** to 3.268 Å in complex **2** is also observed, Table 1. The N–Ni–N and SNi–S angles in complex **1** are acute at 83.6° and 79.6°, while the N–Ni–S angle, within the five-membered ring, is 96.4°. In complex **2**, the \angle N–Ni–N contracts to 77.3°, the \angle S–Ni–S opens to 92.3°, and the \angle N–Ni–S within the five-membered ring contracts to 86.7°.

The dimeric species, [(mmp-mdach) NiCl]₂, **2-Me₂**, is isolated as a hygroscopic, air stable, bright purple powder, which is very soluble in MeOH, H₂O, and MeCN. Thus far crystals have not been obtained; however, conductivity and cyclic voltammetry measurements are similar in **2-Me₂** and **2**, suggesting similar structures. The **2-Me₂** complex was cleaved by imidazole in the preparation of complex **3**.

Synthesis and Structure of [(mmp-mdach)Ni(lm)]Cl, 3

The cleavage of dimeric μ -dithiolato Ni^{II} by monodentate ligands is a fairly common, but not a universally successful, approach to mononuclear square planar nickel complexes. ^{36,39} As shown in Scheme 1, addition of excess imidazole to [(mmp-mdach)NiCl]₂ in MeOH results in an orange solid analyzed as complex 3 in high yield. Complex 3 is hygroscopic, soluble in MeOH, H₂O, and DMF and crystallizes on layering a MeOH solution with Et₂O. The molecular structure of the imidazole-cleaved complex is shown in Figure 3, and significant metric parameters are listed in the figure caption. To our knowledge, 3 provides the first molecular structure of a Ni complex containing both thiolate and imidazole donor ligands. The nickel coordination environment is largely square planar with very slight tetrahedral twist distortion, 7.9°, defined by the intersection of the N(1)Ni(1)N(2) and N(3)-Ni(1)S(1) planes. The N–Ni–N angle within the dach donor is 81.5° while the ∠S–Ni–N_{imid} is 91.4°; the $\angle N(2)$ -Ni(1)-N(3) is 97.1°. Notably, the plane of the imidazole ligand is perpendicular to the $N_2N'SNi$ plane, with the amine N(4) in the imidazole ring on the same side of the $N_2N'S$ coordination plane as is the C_3 portion of the dach ring. As in complexes 1 and 2, the NiN₂C₃ metallodiazacyclohexane ring is in the chair conformation. There is no significant difference in the bond distances of the Ni-Namine and the Ni-Nimid. The Ni-S distance of 2.149(3) Å is shorter than any Ni-S distance of complexes 1 or 2. The extended structure finds a Cl⁻ and MeOH molecule within the unit cell which appear to create a Hbonding network as seen by the Cl $\cdot\cdot\cdot$ O distance of 3.568 Å and Cl $\cdot\cdot\cdot$ N_{imid} distance of 3.119 Å (Figure 4). The latter is well within the summation of van der Waals' radii of chlorine and nitrogen.

Synthesis and Structure of [Ni-1'(CH2-mlm)]Cl, 4

Stoichiometric addition of 4-(chloromethyl)-5-methyl-imidazole · HCl to neutral (bmedach)Ni in MeOH results in solubilization of the insoluble precursors as S-alkylation occurs, Scheme 2. The acidic conditions of the reaction sacrifice a portion of the (bme-dach)Ni starting material; however, use of the acid-free imidazole results in poorer yields. Purified complex 4 was isolated as a rose-colored solid in 30% yield. It is hygroscopic and soluble in

 H_2O , MeOH, and DMF; crystals were grown in a solution of MeOH layered with Et_2O . The solid state structure of **4** (Figure 5) reveals a $(N_2N'S)Ni$ square planar binding motif of two amine nitrogens from the dach ring, the imidazole nitrogen and the thiolate sulfur, with a slightly larger distortion from planarity, a 13.2° Td twist, than was found in complex **3**.

As given in Figure 6, angles and bond distances in complex 4 are similar to those of complex 3. The thioether-S is oriented over the $N_2N'S$ plane, however the N_i - $S_{thioether}$ distance of 3.022 Å is beyond bonding. Although thioethers are weak donors, there are several square planar N_2S_2Ni compounds known in which the sulfur is a thioether within a polydentate ligand or macrocycle. In addition, S-alkylation by reagents that provide an additional binding site is known to maintain the tetradentate N_2S_2 bonding and expand the coordination number of N_2S_2Ni complexes. The switch of the donor atom from the thioether to the N-imidazole in 4 indicates that the greater binding ability of the imidazole nitrogen over the thioether sulfur overwhelms the favorable chelate effect for the thioether, going from a five-membered ring to a less favored eight-membered ring. Scheme 3 outlines likely intermediates (in brackets) in the reaction pathway; neither of these has thus far been verified.

As was also seen in complex 3, the orientation of the imidazole plane in 4 is perpendicular to the $N_2N'S$ plane. The $N(2)\cdots S(1)\cdots C(11)$ linker or imidazole tether is sufficiently long so as not to interfere with the optimal binding of the imidazole donor (vide infra). The closest chloride ions in the crystal lattice are located 3.046 Å away from the N of the imidazole ligand (Supporting Information, Figure S1).

Synthesis and Structure of [(bmlme-dach)Ni](BF₄)₂, 5

Complex **5**, prepared as described in Scheme 4, is isolated as a gold solid that is soluble in MeCN, MeOH, H₂O, and DMF. Figure 7 displays the thermal ellipsoid plot for complex **5** along with alternate views that highlight the slight staggering of the imidazole rings while the NiN₄ plane (Td twist of 7.9°) is largely coplanar with the imidazole ligand planes. The dihedral angle between the planes of the pendant imidazole rings is 11.4°. An analogue of complex **5**, lacking the methyl group on the imidazole and isolated as a perchlorate salt, reported by Bu et al. has similar metric parameters; however, a smaller dihedral angle exists between the imidazole ring planes (6.1°) .³⁷ The extended packing structure of complex **5** shows π – π stacking between imidazole rings as suggested by interplanar distances of 3.432Å (Figure 8). In contrast, the crystal structure of Bu's complex shows the formation of intermolecular hydrogen bonds between the imidazole N–H and the O atom of the ClO₄⁻ counterion resulting in a dimeric structure.³⁷

Despite the differences in the imidazole orientation of the tetradentate $(N_{amine})_2(N_{imid})_2N_i$, complex **5**, and the complexes **3** and **4**, the Ni–N_{imid} bond distances are significantly the same. A final note on the monomeric nickel N₂N'S and N₂N'₂ complexes is in regards to angles within the square plane. Figure 6 shows minor differences in the free imidazole complex **3** and the long tethered imidazole complex **4**. In complex **5**, the $\angle N(1)$ –Ni-N(2) is largely the same as in complexes **3** and **4**, while the angle between donor atoms trans to the diazacycle donors, N(3) and S or N(3) and N(4), opens substantially from 91.4° and 91.6° in **3** and **4**, respectively, to 104° in complex **5**.

Conductivity Measurements

The results of molar conductivity measurements are listed in Table 2. As expected, because of the non-coordinating BF_4^- counterion, complex 2 behaves as a 2:1 electrolyte in both MeCN and H_2O solutions, while the H_2O complex 1, is a 1:1 electrolyte in MeCN and acts as a 2:1 electrolyte in H_2O . Note that the conductivity of **2-Me2** follows that of

complex **1** with a single Cl^- dissociating in the polar organic solvent; both Cl^- ions dissociate in H_2O . The molar conductance values for the mononuclear square planar complexes, **3** and **4**, are consistent with a 1:1 electrolyte in both MeOH and H_2O solutions and complex **5** is a 2:1 electrolyte in MeOH and H_2O .

Electronic Absorption Spectra

Typical square planar nickel complexes exhibit d-d transitions in the range of 400–600 nm. Higher energy and more intense features can be assigned as ligand-to-metal charge transfer (LMCT) transitions. Nickel complexes with RS⁻ ligands show such intense absorbances within the 250–350 nm range, which are attributed to RS⁻ \rightarrow Ni^{II} charge transfer transitions. ⁴³ Table 3 lists the electronic absorption data for complexes **1–5** and **2-Me₂**. The UV–vis absorption spectrum of [(me-mdach)Ni]₂(BF₄)₂, **1**, in which the Ni²⁺ ions are held in a square planar geometry exhibit two d \rightarrow d bands with λ_{max} at 452 and 524 nm, in addition to high energy LMCT absorptions at 229, 252, 305, and 354 nm (ε values >10,000 M⁻¹ cm⁻¹). In complex [(me-mdach)NiCl]₂, **2**, four intense LMCT absorptions are observed and a broad d \rightarrow d band is seen at 527 nm with a shoulder at 490 nm.

The absorptions for **2-Me₂** are similar to complex **2**. The absorption spectrum of the imidazole cleaved dimer, (mmp-mdach)Ni(Im)](Cl), **3**, displays one d-d band with λ_{max} at 467 nm and two intense ligand to metal charge transfer bands at 211 and 288 nm. Similar absorptions are observed for the square planar complex **4**. In complex **5**, all absorptions are of low intensity.

Electronic absorption spectroscopy was used to investigate whether donor switching of the N-imidazole to the S-thioether of Ni-1'(CH₂-mIm)](Cl) might occur during incremental addition of acetic acid to a methanolic solution of **4**, with the expectation that protonated imidazole might promote thioether binding. No changes in the absorption spectrum were observed over a pH range of 8.5 to 3.4, indicating that the coordination environment was constant. These results are consistent with DFT computations which found that the crystallographically observed imidazole bound structure was the isomer of lower energy with an energy difference between the two of 3.34 kcal/mol, Figure 9.

Electrochemical Properties

A summary of electrochemical properties of complexes 1–5, 2-Me₂, and (bme-dach) Ni are given in Table 4. All seven complexes show an irreversible oxidation event, which is ascribed to thiolate oxidation in the case of complexes 3, 4, and (bme-dach)Ni.

The cyclic voltammograms for the N_2S μ -thiolate bridged Ni dimers, 1, 2, and 2-Me₂, are shown in Supporting Information, Figure S2. Two well-defined reduction events are observed in each; the first reduction is reversible when the scan direction is reversed before the second reduction, and is assigned to a Ni^{II}Ni^{II}/Ni^{II}Ni^{II} couple. The second reduction, presumably accessing an unstable Ni^INi^I redox level in the intact dimers, engenders degradation as seen by its irreversibility and also in the differential pulse voltammetry of the first reduction process (Supporting Information, Figure S3). All three dimers display similar electrochemistry in both the anodic and cathodic regimes with differences in potentials relating to the extent of counterion interaction or the presence of gem-dimethyl groups in 2-Me₂

Figure 10 displays the cyclic voltammograms of mononuclear complexes 3–5 and (bmedach)Ni. Figure 10, panels a and b, show fully reversible $\mathrm{Ni^{II}/Ni^{I}}$ reduction events at -1.59 and -2.50 V for complex 5 and (bme-dach) Ni, respectively. The greater accessibility of the former is a result of the dicationic charge, as well as the differences in donor ability of the imidazole versus the thiolate ligands. For complex 4 a reproducible broad feature

(deconvoluting into at least 3 maxima by square wave voltammetry, Supporting Information, Figure S4) is centered at -1.82 V, and a fully reversible reduction is seen at -2.50 V, identical to the Ni^{II}/Ni^I couple of the (bme-dach)Ni dithiolate complex, Figure 10b. Multiple scans did not affect the form of the CV; however, bulk electrolysis of **4** was informative. A potential of -2.26 V was applied to a solution of pure, crystalline complex **4** dissolved in DMF and stopped when the total charge (Q) approached a calculated value of 3 electrons per molecule. The cyclic voltammogram obtained on this solution showed almost total loss of the broad feature at -1.82 V while the reversible wave at -2.50 V and the oxidation wave at -0.18 V remained unchanged, see Supporting Information, Figure S5. The lack of current increase following bulk electrolysis in the -2.50 V event was of concern. As the addition of excess (bme-dach)Ni did not change the intensity or potential of the CV waves, it may be assumed that the solubility limit of (bme-dach)Ni in DMF was reached. This was confirmed by control experiments with pure (bme-dach)Ni.

The low intensity, broad feature centered at -1.82 V in complex 4 and the first two reduction waves in complex 3 (DPV shown in Supporting Information, Figure S6) are tentatively assigned to complexes of different imidazole coordination in number or isomeric form. Consistent with this assignment, on addition of free imidazole to a solution containing complex 3 the multiple events become one broad intense feature centered at about -2.05 V (Supporting Information, Figure S7).

Computational Studies

DFT computational studies were carried out with a goal of determining the activation barrier to imidazole rotation about the Ni–N bond. Using the X-ray crystal structures as a starting point, DFT optimized structures accurately reproduced the experimental coordination geometries, see Supporting Information, Figure S8 and Table S2. Supporting Information, Table S3 lists the energies and compositions of the frontier molecular orbitals of complexes 3 and 4; the corresponding MO contour plots are shown in Figure 11.

The highest-occupied molecular orbitals (HOMOs) of complexes 3 and 4 both display Ni d_{π} – $S_{p\pi}$ antibonding orbital character, with electron density from the Ni d_{yz} (12.3%) and $S_{thiolate}$ p_z (58.8%) orbitals of complex 3; in complex 4, the distribution is Ni d_{yz} (17.1%) and $S_{thiolate}$ p_z (57.1%). The S-thiolate contribution to the HOMO is slightly more in the untethered imidazole derivative, 3, as compared to the tethered imidazole complex, 4, while the Ni orbital contribution is slightly greater in the tethered imidazole compound. Similarly there are small differences between the orbital makeup of the lowest unoccupied molecular orbitals (LUMOs) in complexes 3 and 4, which are in the σ -framework of the molecules. The HOMO–LUMO gaps in complexes 3 and 4 are nearly identical at 3.63 and 3.59 eV, respectively.

The most significant differences in molecular orbitals are observed in the HOMO-1. The HOMO-1 of complex 3 is composed largely of the overlap of the Ni d_z2 (54.0%), Ni s (15.5%) and S_{thiolate} p_y (12.4%) orbitals whereas the HOMO-1 of complex 4 shows a large contribution from the S_{thioether} of 23.4% in addition to the Ni d_{π}-p_{π} overlap.

As discussed above, the S_{thiolate}-Ni interaction dominates the frontier molecular orbitals in complexes **3** and **4**. The N_{imidazole}-Ni bonding interaction is seen in lower lying orbitals which show large contributions of Ni and the N-imidazole character for both the ground and the DFT derived transition state for rotation of the imidazole about the Ni–N bond in complex **3**, vide infra. This interaction will be described in detail in a future publication.

Variable Temperature ¹H NMR Studies

As shown in Figure 6, solid state structures find the orientation of the imidazole ligand plane in both [(mmp-mdach)Ni(Im)]Cl, **3**, and [Ni-1'(CH₂-mIm)]Cl, **4**, to be perpendicular to the NiN₂N'S plane and largely eclipsing the N–Ni–N' vector. To further explore the imidazole ligand orientational preference, the solution phase conformation of the imidazole ligand in complex **3** was investigated via variable temperature 1 H NMR spectroscopy. At 23 °C, the spectrum of **3** in CD₃OD shows three sharp singlets attributed to the C–H hydrogens on the coordinated imidazole ligand positioned at 8.11, 7.33, and 7.12 ppm, Figure 12. The assignments given in Figure 12 are in agreement with DFT computations, vide infra (Supporting Information, Figure S9). Upon lowering the temperature, resonances *a* and *b* broaden and by -80 °C each have split into two signals, indicating the presence of two isomers. Integration shows *a'* and *a''* to be in a ratio of ~1. The resonance due to the proton labeled *c* remains sharp throughout the temperature range, and the resonances derived from *b* overlap with *c* and an impurity. Note that impurities are readily seen at room temperature. The lower field impurity is unaffected by temperature changes. However, the higher field impurity, which has not been identified, undergoes broadening as do the signals of interest.

Thermodynamic (isomer ratios) and kinetic barriers associated with the fluxional process were obtained by using conventional equations, eqs 1 and 2.

$$\Delta G^{\circ} = -RT \ln(K_{eq}), \quad K_{eq} = [a']/[a'']$$
 (1)

$$\Delta G = -RT \ln(k_{\rm T} h/k_{\rm b} T_{\rm coal}), \quad k_{\rm T} = (\pi \Delta \nu/2)$$
(2)

The ratio of the two isomers (57:43) at -80 °C (193 K) resulted in a ΔG ° of 0.2 kcal mol⁻¹. From the chemical shift difference of a' and a'' (164.7 Hz) and the coalescence temperature (213 K), eq 2 gives ΔG^{\ddagger} equal to 8.9 kcal mol⁻¹.

There are four possible isomers of 3 (Figure 13). Isomer $\bf A$ depicts the molecular structure as determined by X-ray crystallography. Isomer $\bf B$ leaves the imidazole orientation unchanged but the NiN₂C₃ metallocyclooctane ring is converted from chair to boat conformation. Isomers $\bf C$ and $\bf D$ are analogous to $\bf A$ and $\bf B$, respectively, but with the imidazole ring inverted. While the lowest energy gas phase DFT-calculated structure is isomer $\bf C$, solvent correction indicates that in MeOH isomer $\bf A$, the experimentally found structure, is of lowest energy (more stable than $\bf C$ by 0.68 kcal/mol). The stability of $\bf A$ in polar solvent over $\bf C$ is attributed to the differences of the dipole moments of the two complexes; the dipole moment in $\bf A$ is calculated to be 6.59 and in $\bf B$ it is 6.11. In both the gas phase and in solvent, the calculated difference in energy between the two complexes is relatively small. DFT calculations were used to examine activation barriers to proton site equilibration due to the ring flip in the diazacycle backbone ($\bf A$ vs $\bf B$ or $\bf C$ vs $\bf D$) or to rotation of the coordinated imidazole ($\bf A$ vs $\bf C$ or $\bf B$ vs $\bf D$).

Note that the calculated ΔG° value of isomers **A** versus **B** and **C** versus **D** would correspond to an isomer ratio of ~33,000:1 and ~700:1, respectively. At these ratios, only one set of signals in the NMR spectra would be observable at low temperatures. On the basis of these values, the fluxional process that most likely corresponds to the signals seen in the NMR spectra is the rotation of the imidazole ring that equilibrates isomers **A** and **C**.

The DFT calculated barriers for the processes that interconvert the four isomers are given in Figure 14. As shown in Figure 14a, starting from the structure of 3 determined crystallographically, isomer **A**, the DFT calculated ΔG^{\ddagger} for the ring flip in the diazacycle backbone from the chair to the boat conformation, achieving a transition state where the C_3 N to N linker is fairly flat, is 7.02 kcal mol⁻¹. Calculations carried out for the ring flip of the isomer with the imidazole rotated 180° as compared to the solid state structure, isomer **B**, resulted in a ΔG^{\ddagger} of 6.59 kcal mol⁻¹ (Figure 14(b)). The DFT-calculated ΔG^{\ddagger} of 8.86 kcal mol⁻¹ for the conversion of isomer **A** to **C**, that is, rotation of the imidazole as seen in Figure 14c, passing through a transition state where the imidazole plane is roughly within the NiN₂S plane, is strikingly similar to the experimental value obtained from the VT NMR study. Thus, the DFT calculations that aid interpretation of experimental results suggest that the separate isomers seen at low temperature are due to cessation of imidazole rotation about the Ni–N bond. Furthermore, the calculations suggest there is little difference in energy between the two rotational isomers of 3 (<0.2 kcal mol⁻¹), and this is also indicated in the experimental ¹HNMRdata which by the ratio of isomers is about 1 at -80 °C.

Reactivity Studies with Small Molecules (O2-, O2, and H2O2)

Complexes 3–5 have been examined for superoxide reactivity using the nitroblue tetrazolium (NBT) assay. This qualitative test based on the reduction of NBT by O_2^- is detected by the change of colorless NBT to the blue formazan (λ_{max} =580 nm, ~30 000 M⁻¹ cm⁻¹; Figure 15).⁴⁴ The presence of an active SOD inhibits the color formation by scavenging the O_2^- radical. Figure 16 shows the results of addition of solid KO₂ (100 equiv per mole of NBT) to a (61 μ M) aqueous NBT solution (phosphate buffer, pH 7.4). Note that the limited solubility of formazan in aqueous solution causes a decrease in the absorbance over time.

Under the same conditions employed in the control experiment and in the presence of complex 3 (69 μ M), a 40% decrease in the intensity of the band centered at 580 nm was observed, indicating a decrease in formazan production (Figure 17a). This result suggests that 3 possesses superoxide scavenging properties that prevent a portion of the NBT from reacting withO₂⁻ and at a rate competitive with NBT. In addition, intense bubble formation, much more than with formazan in the absence of 3, was observed within the first 30 s following KO₂ addition. It should be noted that there is no indication of catalytic O₂⁻ decomposition. The addition of solid KO₂ to concentrated solutions of complex 3, resulted in a shift in the d-d band from 464 to 471 nm and a new band appeared at 350 nm (Figure 17b), suggesting that a new nickel species is formed.

The ability of complexes **4** and **5**, and (bme-dach)Ni, as well as NiCl₂, to inhibit NBT superoxide reactivity was screened by identical experiments. Under both low and high concentrations, none inhibited the production of formazan.

Complex 3 was screened for reactivity with the products of superoxide dismutation, O_2 and H_2O_2 . Molecular oxygen was bubbled through a MeOH solution of complex 3. No oxygenation products were observed, and only the starting material was recovered. Upon addition of H_2O_2 (10 mM) to complex 3 dissolved in MeOH, an immediate color change from orange to yellow was observed. The molecular formulas and predicted isotope envelopes for both the mono-oxygenated and bis-oxygenated derivatives of complex 3 were observed in the ESI-MS spectrum (Supporting Information, Figure S10). These results indicate that complex 3 is stable to aerobic oxidation, and only strong oxidants are capable of oxidizing the Ni-bound $N_2N'S$ ligand.

Summary and Remarks

Complexes 3 and 4 presented above are, to our knowledge, the first molecular structures of compounds containing both an S-thiolate and N-imidazole donor atom in the first coordination sphere of $\mathrm{Ni^{II}}$. The use of the (bme-dach)Ni complex and the dimeric dithiolate bridged $\mathrm{Ni^{II}}$ dication as precursor reagents in the preparation of the $\mathrm{Ni(N_2N'S)}$ complexes resulted in similar solid state structures for complexes containing both tethered and untethered imidazole ligands. That the diazacycloheptane $\mathrm{N_2}$ "backbone" plays a stabilizing role in these complexes is highly reasonable. The following salient points are to be noted.

Imidazole Ligand Geometrical Orientation in Square Planar Ni^{II} Complexes

While severe ligand restrictions position the imidazole ligand coplanar with the $N_2N'_2Ni^{II}$ plane of complex **5**, the solid state structures of complexes **3** and **4** revealed a preferred orientation of the imidazole donor ligand perpendicular to the $N_2N'SNi^{II}$ plane. The solution phase VT ^{1}H NMR study of complex **3** demonstrated that the imidazole ligand freely rotates about the Ni–N_{imid} bond at 22 $^{\circ}C$, with static structures appearing between -60 and -80 $^{\circ}C$. Both the experimental and the DFT computed barriers to rotation are found to be \sim 9 kcal mol $^{-1}$. The lowest energy DFT-calculated gas phase structure also found the imidazole plane to orient perpendicular to the N₂N'S plane, but rotated 180° with respect to the crystallographically determined structure. Applying solvent corrections, the DFT lowest energy structure was calculated to be the same orientation as observed in the solid state. Thus, the built-in asymmetry of the diazacycloheptane ring provides subtle tuning of ligand orientation preferences.

The orientation of imidazole ligands in metalloenzyme active sites is well recognized to influence structure/function relationships such as midpoint redox potentials, electronic structure, spin states, electron transfer rates, and the coordination of substrates. 45 Furthermore, ligand rotational properties have been shown to contribute to significant factors affecting antitumor properties in ruthenium antitumor compounds. 46 The DFT computed transition state structure for imidazole rotation about the Ni–Nimid bond in complex 3 positions the imidazole ligand roughly coplanar with the NiN2S plane. In fact, elongation of the Nimidazole-Ni bond distance by 0.06A(from 1.922 in the DFT calculated ground state to 1.982 Å in the transition state) is accompanied by distortion (a Td twist defined by the intersection of the N2Ni and SNimidNi planes, of 21.2°), Figure 18. The preferred orientation may be a product of steric and/or electronic effects, studies of which are currently in progress.

Superoxide Reactivity

The nickel-imidazole complexes described above are all water-soluble and thus their potential for superoxide reactivity could be assessed in aqueous buffer via the NBT assay. Only complex 3 competed with the NBT scavenging of superoxide; complexes 4, 5, and (bme-dach)Ni did not and neither did simple salts such as NiCl₂. As the NBT assay gives little information regarding the nature of interference from the coordination complex, we can regard these results as preliminary. This suggests the need for further examination of nickel complexes of various charge and redox properties such as we have in a catalog of such square planar Ni complexes.

Implications to Nickel Containing Biomolecules

An unsuccessful attempt was made to synthesize a NiSOD enzyme active site model complex from alkylation of a thiolate within an $N_2S_2Ni^{II}$ framework by chloromethylimidazole to thus incorporate a dangling imidazole (His mimic) with the capability of shifting into an axial binding position on oxidation of Ni^{II} to Ni^{III} . The resulting N_2N

'Sthiolate binding motif found for complex **4**, which matched that of complex **3**, was impressive of the good binding ability of imidazole nitrogen and its preference for the square plane of Ni^{II}. In the NiSOD enzyme active site, the axial His binding is governed by the protein superstructure, the position of the His residue next to the N-terminus that provides the amine ligation, the coordination of the strong carboxyamido N and S donors of one cysteine unit, and a second distal S-cysteine donor. This square planar coordination environment creates two favorable 5-membered rings, whereas the His ligand binding in the square plane in place of the N-terminus amine would result in one 5-membered ring and a less-favored 7-membered ring.

Interestingly, the $(N_{imid})_3NiS_{cys}$ "plane" of NikR, Figure 1, finds a range of N_{imid} plane orientations, canted so as to best accommodate the steric requirements. As nickel binding or release, with concomitant long-range protein structural changes, is an important feature of this site, specific orientations of the imidazole ligands are likely suspects as triggers of release and binding. Drennan, Zamble, and co-workers have demonstrated that other metal ions may bind in this site; however, the nickel form is reported to be $250 \times$ more active. 11b, 47 Our $(N_2N'S)Ni$ complexes are suitable as first coordination sphere molecular models of the Ni-binding site of the Nik-R protein and are expected to be useful for selectivity and relative binding affinity studies of physiologically relevant metal ions.

Supplementary Material

Refer to Web version on PubMed Central for supplementary material.

Acknowledgments

We gratefully acknowledge the financial support of the National Science Foundation (CHE-0616695 to M.Y.D.) with contributions from the R. A. Welch Foundation (A-0924) and the National Institutes of Health (Chemistry-Biology Interface Training Grant to R.J., T32 GM008523). The assistance of Cody Carson with the X-ray Crystallography is much appreciated as are extensive conversations with Prof. Michael B. Hall.

References

- (a) Farmer PJ, Reibenspies JH, Lindahl PA, Darensbourg MY. J Am Chem Soc 1993;115:4665–4674.
 (b) Musie G, Farmer PJ, Tuntulani T, Reibenspies JH, Darensbourg MY. Inorg Chem 1996;35:2176–2183. [PubMed: 11666411]
- 2. (a) Smee JJ, Miller ML, Grapperhaus CA, Reibenspies JH, Darensbourg MY. Inorg Chem 2001;40:3601–3605. [PubMed: 11421712] (b) Golden ML, Whaley CM, Rampersad MV, Reibenspies JH, Hancock RD, Darensbourg MY. Inorg Chem 2005;44:875–883. [PubMed: 15859264]
- 3. Green KN, Brothers SM, Jenkins RM, Carson CE, Grapperhaus CA, Darensbourg MY. Inorg Chem 2007;46:7536–7544. [PubMed: 17685511]
- (a) Kruger HJ, Peng G, Holm RH. Inorg Chem 1991;30:734–742. (b) Sellmann D, Prechtel W, Knoch F, Moll M. Z Naturforsch (B) 1992;47:1411–1423. (c) Wang Q, Blake AJ, Davies ES, McInnes EJL, Wilson C, Schroder M. Chem Commun 2003:3012–3013. (d) Hatlevik O, Blanksma MC, Mathrubootham V, Arif AM, Hegg EL. J Biol Inorg Chem 2004;9:238–246. [PubMed: 14735332] (e) Grapperhaus CA, Mullins CS, Kozlowski PM, Mashuta MS. Inorg Chem 2004;43:2859–2866. [PubMed: 15106973] (f) Krishnan R, Riordan CG. J Am Chem Soc 2004;126:4484–4485. [PubMed: 15070343] (g) Bouwman E, Reedijk J. Coord Chem Rev 2005;249:1555–1581. (h) Chohan BS, Maroney MJ. Inorg Chem 2006;45:1906–1908. [PubMed: 16499349] (i) Harrop TC, Olmstead MM, Mascharak PK. Inorg Chem 2006;45:3424–3436. [PubMed: 16602803] (j) Rauchfuss TB. Science 2007;316:553–554. [PubMed: 17463276] (k) Shearer J, Dehestani A, Abanda F. Inorg Chem 2008;47:2649–2660. [PubMed: 18330983]
- 5. (a) Sugiura Y, Hirayama Y. J Am Chem Soc 1977;99:1581–1585. [PubMed: 839006] (b) Sugiura Y. Inorg Chem 1978;17:2176–2182.

(a) Tesfai TM, Green BJ, Margerum DW. Inorg Chem 2004;43:6726–6733. [PubMed: 15476372]
 (b) Burrows CJ, Perez RJ, Muller JG, Rokita SE. Pure Appl Chem 1998;70:275–278.

- 7. Ross SA, Burrows CJ. Inorg Chem 1998;37:5358-5363.
- 8. Van Horn JD, Bulaj G, Goldenberg DP, Burrows CJ. J Biol Inorg Chem 2003;8:601–610. [PubMed: 12827456]
- 9. Barondeau D, Kassmann C, Bruns C, Tainer J, Getzoff E. Biochem 2004;43:8038–8047. [PubMed: 15209499]
- Wuerges J, Lee J, Yim Y, Yim H, Kang S, Carugo KD. Proc Natl Acad Sci USA 2004;101:8569– 8574. [PubMed: 15173586]
- (a) Schreiter ER, Sintchak MD, Guo Y, Chivers PT, Sauer RT, Drennan CL. Nat Struct Biol 2003;10:794–799. [PubMed: 12970756] (b) Schreiter ER, Wang SC, Zamble DB, Drennan CL. Proc Natl Acad Sci USA 2006;103:13676–13681. [PubMed: 16945905]
- (a) De Pina K, Desjardin V, Mandrand-Berthelot MA, Giordano G, Wu LF. J Bacteriol
 1999;181:670–674. [PubMed: 9882686] (b) Chivers PT, Sauer RT. J Biol Chem 2000;275:19735–19741. [PubMed: 10787413]
- 13. (a) Chivers PT, Sauer RT. Chem Biol 2002;9:1141–1148. [PubMed: 12401498] (b) Wang SC, Dias AV, Bloom SL, Zamble DB. Biochemistry 2004;43:10018–10028. [PubMed: 15287729]
- (a) Youn HD, Kime EJ, Roe JH, Hah YC, Kang SO. Biochem J 1996;318:889–896. [PubMed: 8836134]
 (b) Youn HD, Youn H, Lee JW, Yim YI, Lee JK, Hah YC, Kang SO. Arch Biochem Biophys 1996;334:341–348. [PubMed: 8900409]
- (a) Fiedler AT, Bryngelson PA, Maroney MJ, Brunold TC. J Am Chem Soc 2005;127:5449–5462.
 [PubMed: 15826182] (b) Mullins CS, Grapperhaus CA, Kozlowski PM. J Biol Inorg Chem 2006;11:617–625.
 [PubMed: 16724228]
- (a) Shearer J, Long LM. Inorg Chem 2006;45:2358–2360. [PubMed: 16529443] (b) Shearer J,
 Zhao N. Inorg Chem 2006;45:9637–9639. [PubMed: 17112256]
- Ma H, Cattopadhyay S, Petersen JL, Jensen MP. Inorg Chem 2008;47:7966–7968. [PubMed: 18710223]
- 18. Neupane KP, Shearer J. Inorg Chem 2006;45:10552–10566. [PubMed: 17173410]
- 19. Pelmenschikov V, Siegbahn PEM. J Am Chem Soc 2006;128:7466–7475. [PubMed: 16756300]
- Neupane KP, Gearty K, Francis A, Shearer J. J Am Chem Soc 2007;129:14605–14618. [PubMed: 17985883]
- 21. Snyder HR, Stewart JM, Aeigler JB. J Am Chem Soc 1947;69:2672. [PubMed: 20270817]
- 22. Rosen T, Nagel AA, Rizzi JP, Ives JL, Daffeh JB, Ganong AH, Guarino K, Heym J, McLean S, Nowakowski JT, Schmidt AW, Seeger TF, Siok CJ, Vincent LA. J Med Chem 1990;33:2715–2720. [PubMed: 2213824]
- 23. SMART 1000 CCD. Bruker Analytical X-ray Systems; Madison, WI: 1999.
- 24. Sheldrick, G. SHELXTL-PLUS, reVision 4.11 V, SHELXTL-PLUS Users Manual. Siemens Analytical X-ray Instruments, Inc; Madison, WI: 1990.
- 25. Sheldrick, G. SHELXS-97, Program for Crystal Structure Solution. Universität Göttingen; Göttingen, Germany: 1997.
- Sheldrick, G. SHELXL-97, Program for Crystal Structure Refinement. Universität Göttingen; Göttingen, Germany: 1997.
- 27. Cerius², version 4.10. Accelrys Inc; San Diego, CA: 2007.
- 28. Becke AD. J Chem Phys 1993;98:5648-5652.
- 29. Lee C, Yang W, Parr RG. Phys Rev 1998;37:785-789.
- 30. All calculations were carried out with the Gaussian 03 program: Frisch, MJ., et al. Gaussian 03, revision C.02. Gaussian Inc: Wallingford, CT; 2004. See Supporting Information for the full reference.
- 31. Dolg M, Wedig U, Stoll H, Preuss H. J Chem Phys 1987;86:866–872.
- 32. (a) Hay PJ, Wadt WR. J Chem Phys 1985;82:284–398. (b) Hay PJ, Wadt WR. J Chem Phys 1985;82:270–283.

33. Hŏllwarth A, Böhme M, Dapprich S, Ehlers AW, Gobbi A, Jonas V, Köhler KF, Stegmann R, Veldkamp A, Frenking G. Chem Phys Lett 1993;208:237–240.

- 34. Dunning TH Jr. J Chem Phys 1989;90:1007-1023.
- 35. (a) Hehre WJ, Ditchfield R, Pople JA. J Chem Phys 1972;56:2257–2261. (b) Hariharan PC, Pople JA. Theor Chim Acta 1973;28:213–222. The d',p' functions are the exponents from the 6-311G(d,p) basis set: (c) Krishnan R, Binkley JS, Seeger R, Pople JA. J Chem Phys 1980;72:650–654.
- 36. Grapperhaus CA, Bellefuille JA, Reipenspies JH, Darensbourg MY. Inorg Chem 1999;38:3698–3703. [PubMed: 11671129]
- 37. (a) Du M, Guo YM, Bu XH, Ribas J, Monfort M. New J Chem 2002;26:939–945. (b) Guo YM, Du M, Bu XH. Inorg Chim Acta 2005;358:1887–1896.
- 38. (a) Colpas GJ, Kumar M, Day RO, Maroney MJ. Inorg Chem 1990;29:4779–4788. (b) Linck RC, Spahn CW, Rauchfuss TB, Wilson SR. J Am Chem Soc 2003;125:8700–8701. [PubMed: 12862445] (c) Wang Q, Blake AJ, Davies ES, McInnes EJL, Wilson C, Schroder M. Chem Commun 2003:3012–3013. (d) Krishnan R, Riordan CG. J Am Chem Soc 2004;126:4484–4485. [PubMed: 15070343] (e) Rao PV, Bhaduri S, Jiang J, Holm RH. Inorg Chem 2004;43:5833–5849. [PubMed: 15360232] (f) Harrop TC, Olmstead MM, Mascharak PK. Inorg Chem 2006;45:3424–3436. [PubMed: 16602803] (g) Redin K, Wilson AD, Newell R, DuBois MR, DuBois DL. Inorg Chem 2007;46:1268–1276. [PubMed: 17249658]
- 39. (a) Kruger HJ, Holm RH. Inorg Chem 1989;28:1148–1155. (b) Mirza SA, Pressler MA, Kumar M, Day RO, Maroney MJ. Inorg Chem 1993;32:977–987. (c) Sellman D, Prechtel W, Knoch F, Moll M. Inorg Chem 1993;32:538–546. (d) Sellman D, Huabinger D, Heinemann FW. Eur J Inorg Chem 1999:1715–1725.(e) Huang, D.; Deng, L.; Sun, J.; Holm, RH. Inorg Chem. ASAP; 2009.
- (a) Blinn E, Busch DH. J Am Chem Soc 1968;90:4280–4285.
 (b) Musie G, Reibenspies JH, Darensbourg MY. Inorg Chem 1998;37:302–310.
- 41. (a) Goodman DC, Reibenspies JH, Goswami N, Jurisson S, Darensbourg MY. J Am Chem Soc 1997;119:4955–4963. (b) Smee JJ, Goodman DC, Reibenspies JH, Darensbourg MY. Eur J Inorg Chem 1999:539–546.
- 42. Geary WJ. Coord Chem Rev 1971;7:81-122.
- 43. Lever, ABP. Inorganic Electronic Spectroscopy. 2. Elsevier; New York: 1984.
- 44. Greenwald, RA. CRC Handbook of Methods for Oxygen Radical Research. CRC Press; Boca Raton, FL: 1985. p. 65-69.
- 45. (a) Chipman DM, Scheidt WR. J Am Chem Soc 1986;108:1163–1167. (b) Wang X, Berry SM, Xia Y, Lu Y. J Am Chem Soc 1999;121:7449–7450. (c) Glastyan AS, Zaric SD, Knapp EW. J Biol Inorg Chem 2005;10:343–354. [PubMed: 15843984]
- 46. Velders AH, Quiroga AG, Haasnoot JG, Reedijk J. Eur J Inorg Chem 2003:713–719.
- 47. Bloom SL, Zamble DB. Biochem 2004;43:10029-10038. [PubMed: 15287730]

Figure 1. Metal binding site of NikR and the active site of NiSOD. 9–11

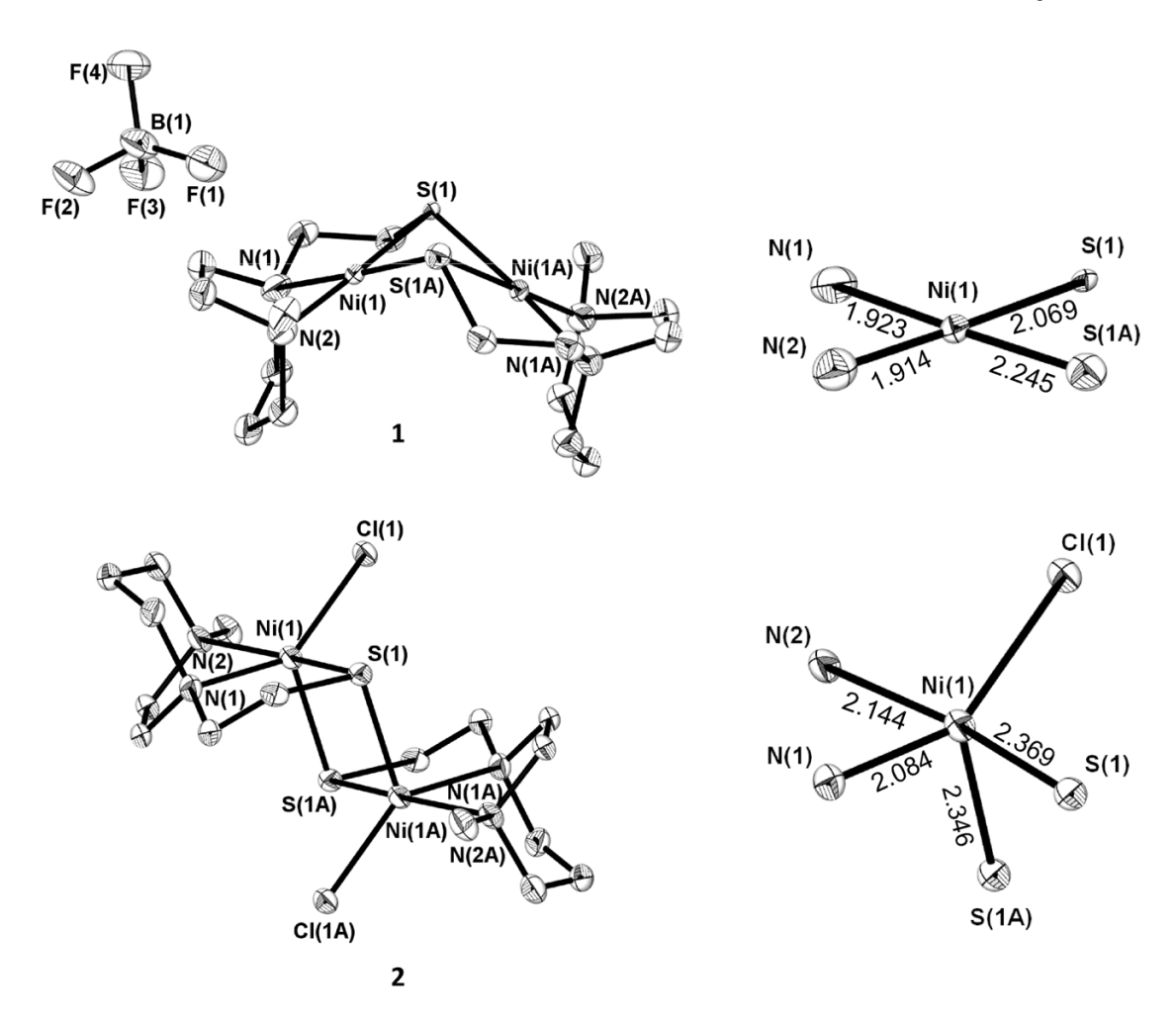


Figure 2.

Molecular structure of complexes 1 and 2 shown as thermal ellipsoids at 50% probability. First coordination spheres shown at right.

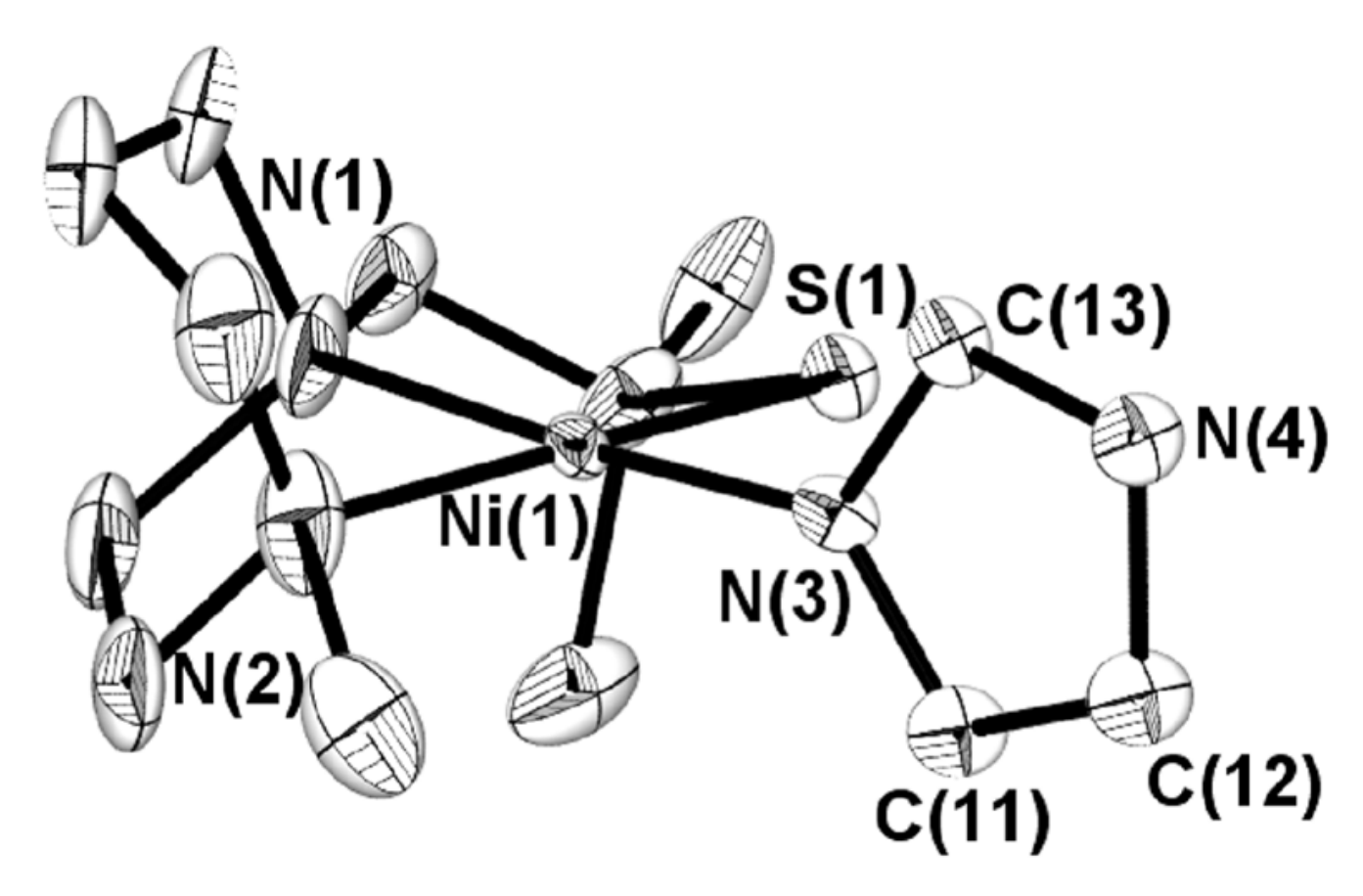


Figure 3. Molecular structure of the cation of **3** shown as thermal ellipsoids at 50% probability. The Cl $^-$ counterion and MeOH molecule are not shown. Selected bond lengths (Å): Ni(1)–S(1), 2.149(3); Ni(1)–N(1), 1.897(10); Ni(1)–N(2), 1.949(10); Ni(1)–N(3), 1.888(9); N(3)–C(13), 1.342(12); N(3)–C(11), 1.372(13); N(4)–C(13), 1.326(13); N(4)–C(12), 1.413(13); C(11)–C(12), 1.316(14). Selected bond angles (deg): N(1)–Ni(1)–N(2), 81.5(5); N(1)–Ni(1)–S(1), 90.4(3); N(2)–Ni(1)–N(3), 97.1; S(1)–Ni(1)–N(3), 91.4(3); N(1)–Ni(1)–N(3), 175.5(4); N(2)–Ni(1)–S(1), 170.6(4).

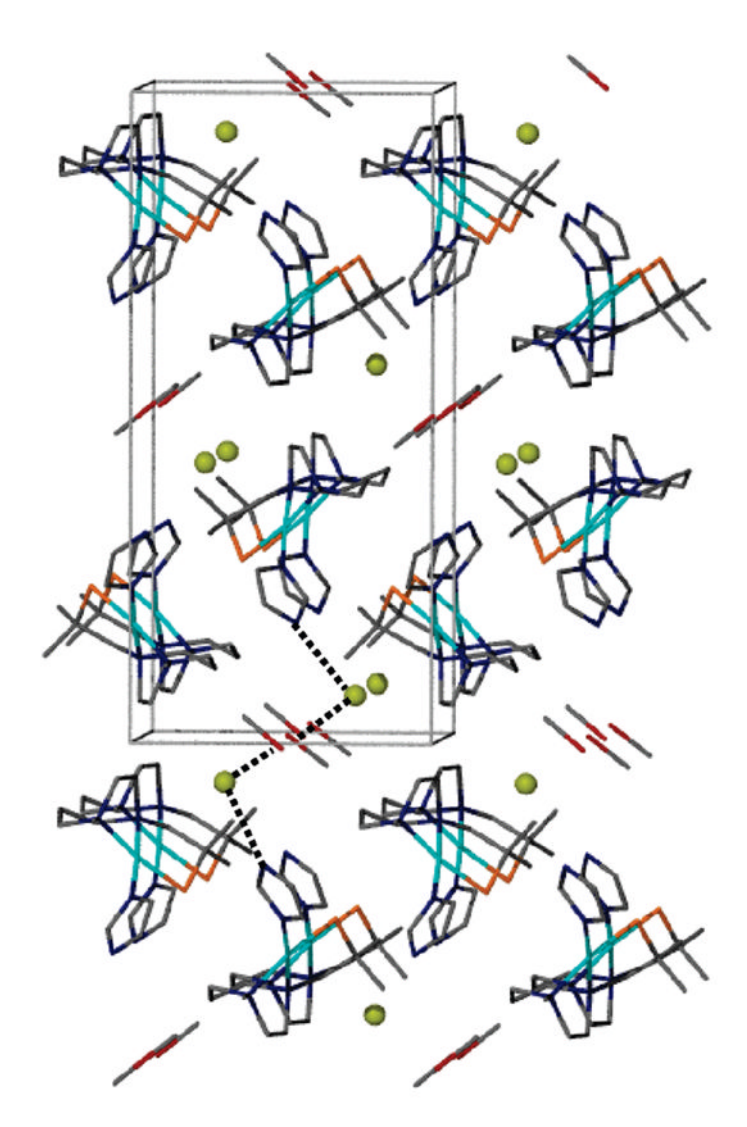


Figure 4. Packing diagram of complex **3**.

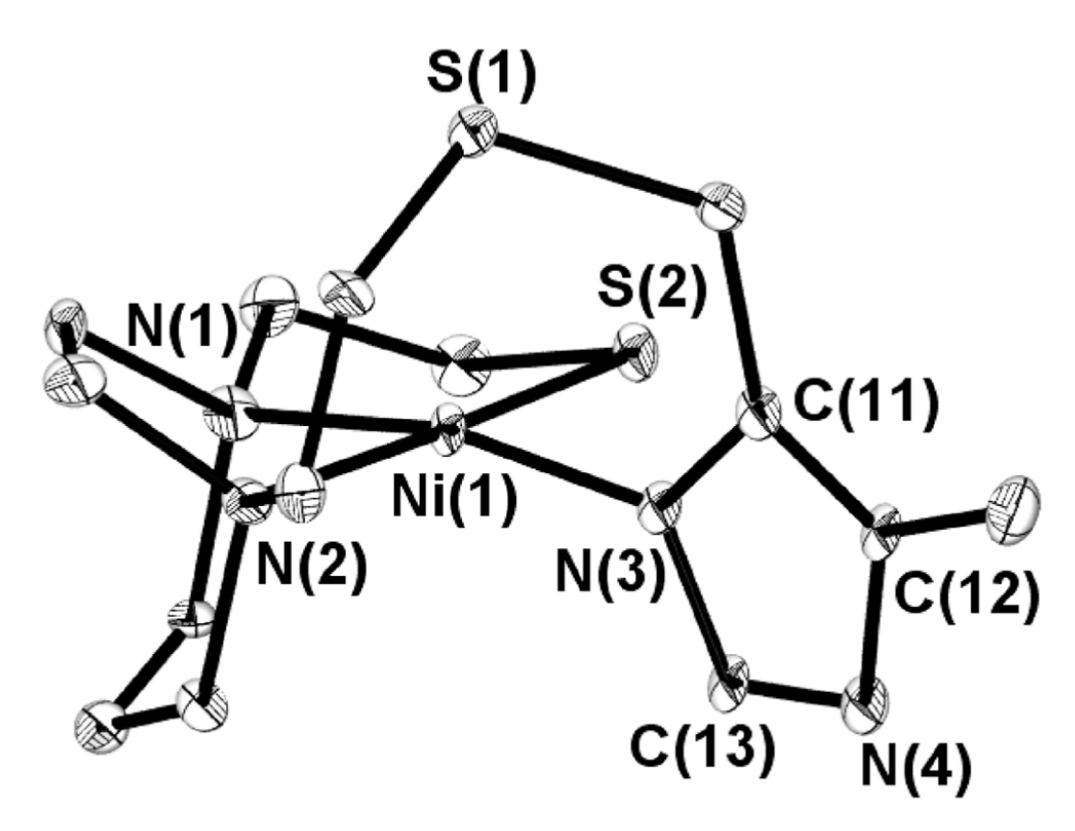


Figure 5. Molecular structure of the cation of **4** shown as thermal ellipsoids at 50% probability. The Cl $^-$ counterion is not shown. Selected bond lengths (Å): Ni(1)–S(2), 2.168(2); Ni(1)–N(1), 1.906(7); Ni(1)–N(2), 1.995(5); Ni(1)–N(3), 1.908(9); N(3)–C(13), 1.322(8);N(3)–C(11), 1.378(10); N(4)–C(13), 1.336(10); N(4)–C(12), 1.381(9); C(11)–C(12), 1.324(11). Selected bond angles (deg): N(1)–Ni(1)–N(2), 82.3(3); N(1)–Ni(1)–S(2), 90.3(2); N(2)–Ni(1)–N(3), 95.5(3); S(2)–Ni(1)–N(3), 91.6(2).

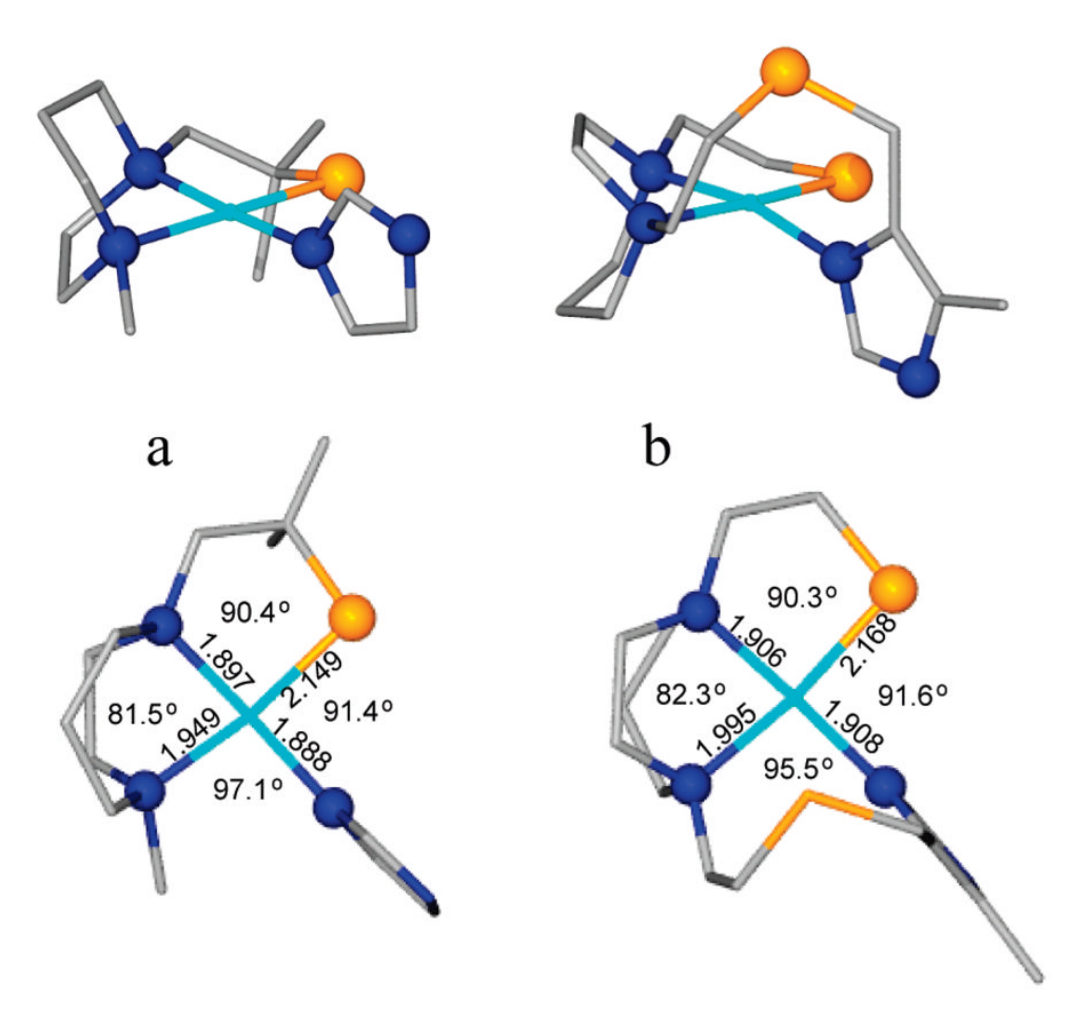


Figure 6. Ball and stick drawings of (a) [(mmp-mdach)Ni(Im)]Cl, 3, and (b) [Ni-1'(CH₂-mIm]Cl, 4. Counter anions are not shown. Top: side view; Bottom: View \bot to N₂S plane with selected metric parameters.

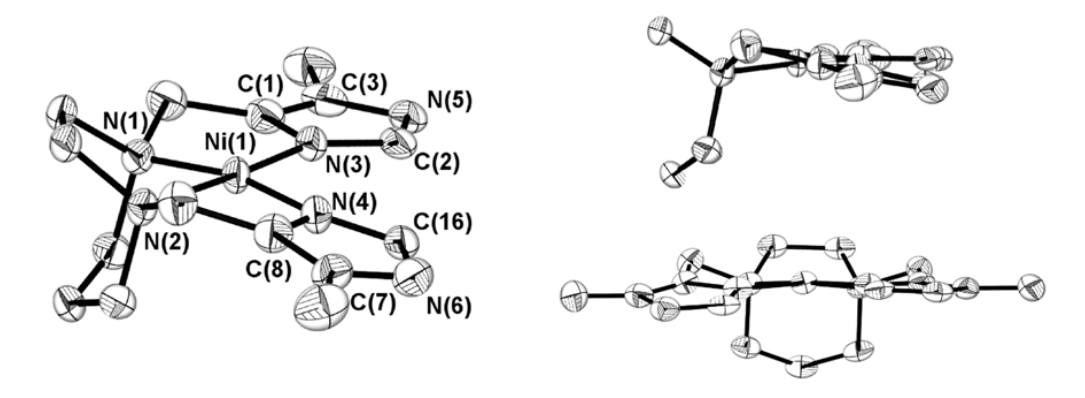


Figure 7. Molecular structure of the dication of **5** shown as thermal ellipsoids at 50% probability. The BF₄ counterions are not shown. Selected bond lengths (Å): Ni(1)–N(1), 1.913(3); Ni(1)–N(2), 1.904(3); Ni(1)–N(3), 1.873(3); Ni(1)–N(4), 1.894(3); N(3)–C(1), 1.373(5); N(3)–C(2), 1.332(5); N(5)–C(2), 1.334(5); N(5)–C(3), 1.377(6); C(1)–C(3), 1.376(6); N(4)–C(8), 1.386(5); N(4)–C(16), 1.339(5); N(6)–C(7), 1.383(6); N(6)–(C16), 1.342(6); C(7)–C(8), 1.359(6). Selected bond angles (deg): N(1)–Ni(1)–N(2), 83.3(2); N(3)–Ni(1)–N(4), 104.1(2); N(1)–Ni(1)–N(3), 86.5(2); N(2)–Ni(1)–N(4), 85.8(2); N(1)–Ni(1)–N(4), 167.0(2); N(2)–Ni(1)–N(3), 169.6(2).

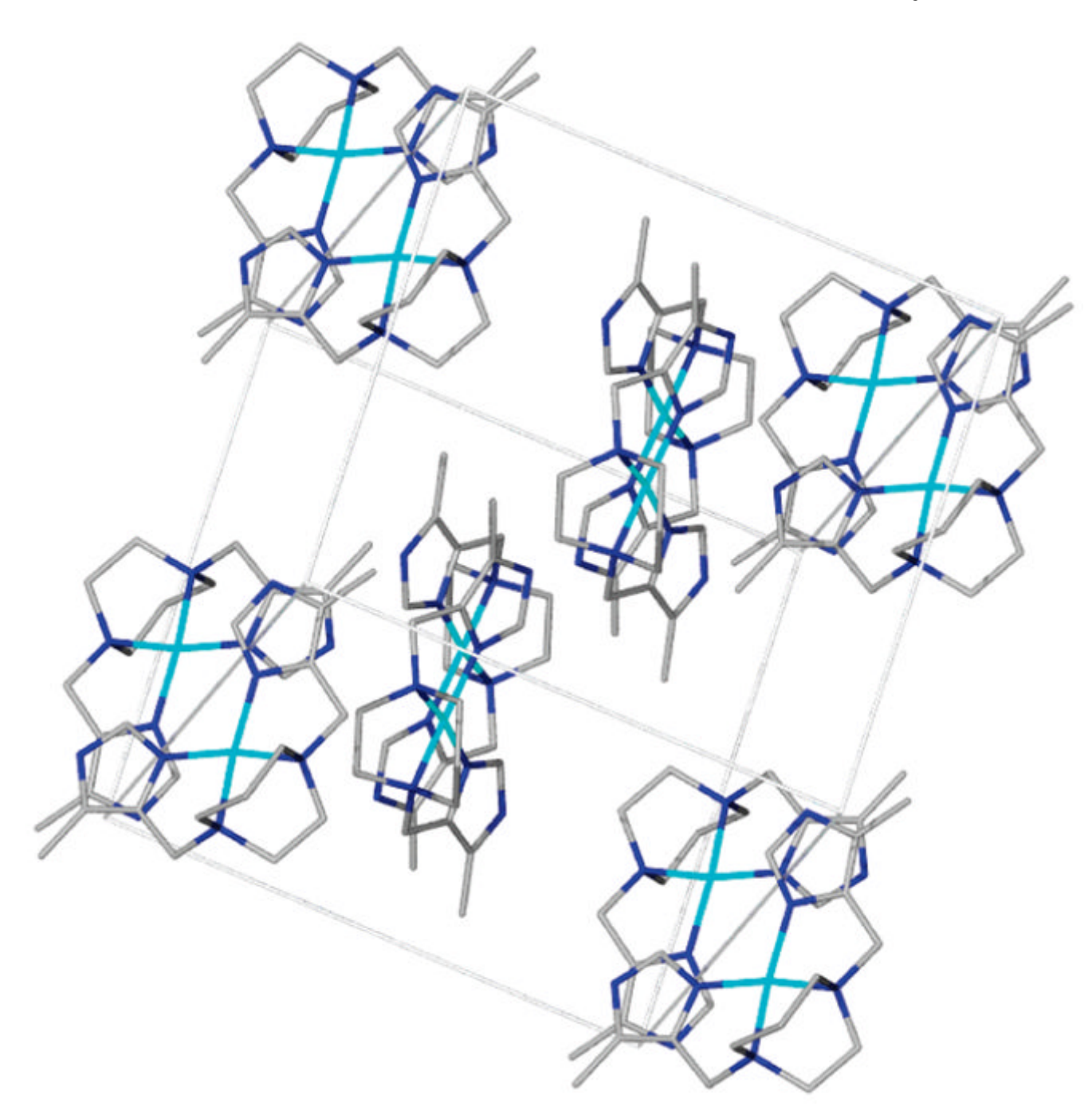


Figure 8. Packing diagram of complex **5** showing π – π stacking between imidazole rings.

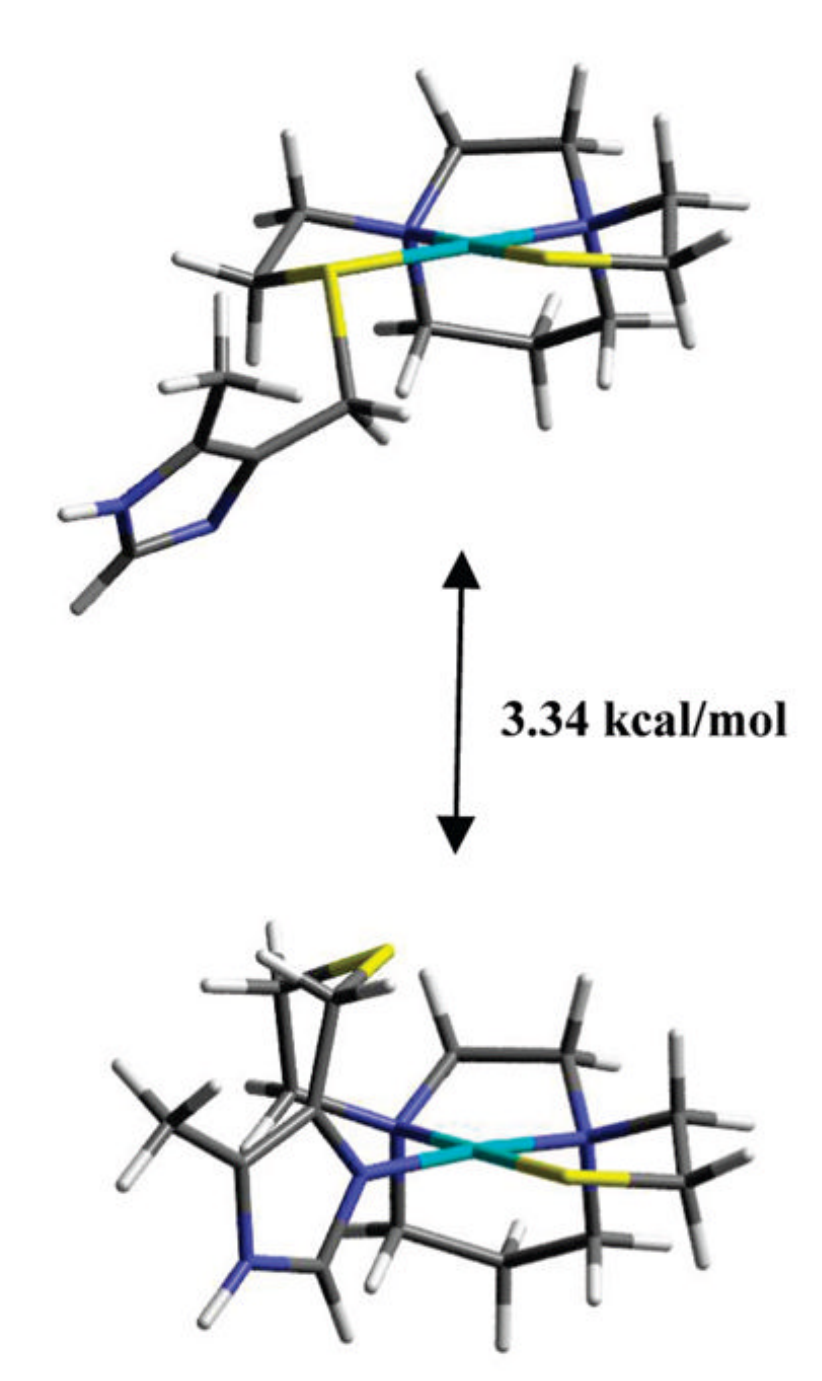


Figure 9.DFT optimized isomeric forms of complex **4**. (top) S-thioether bond (bottom) N-imidazole bound.

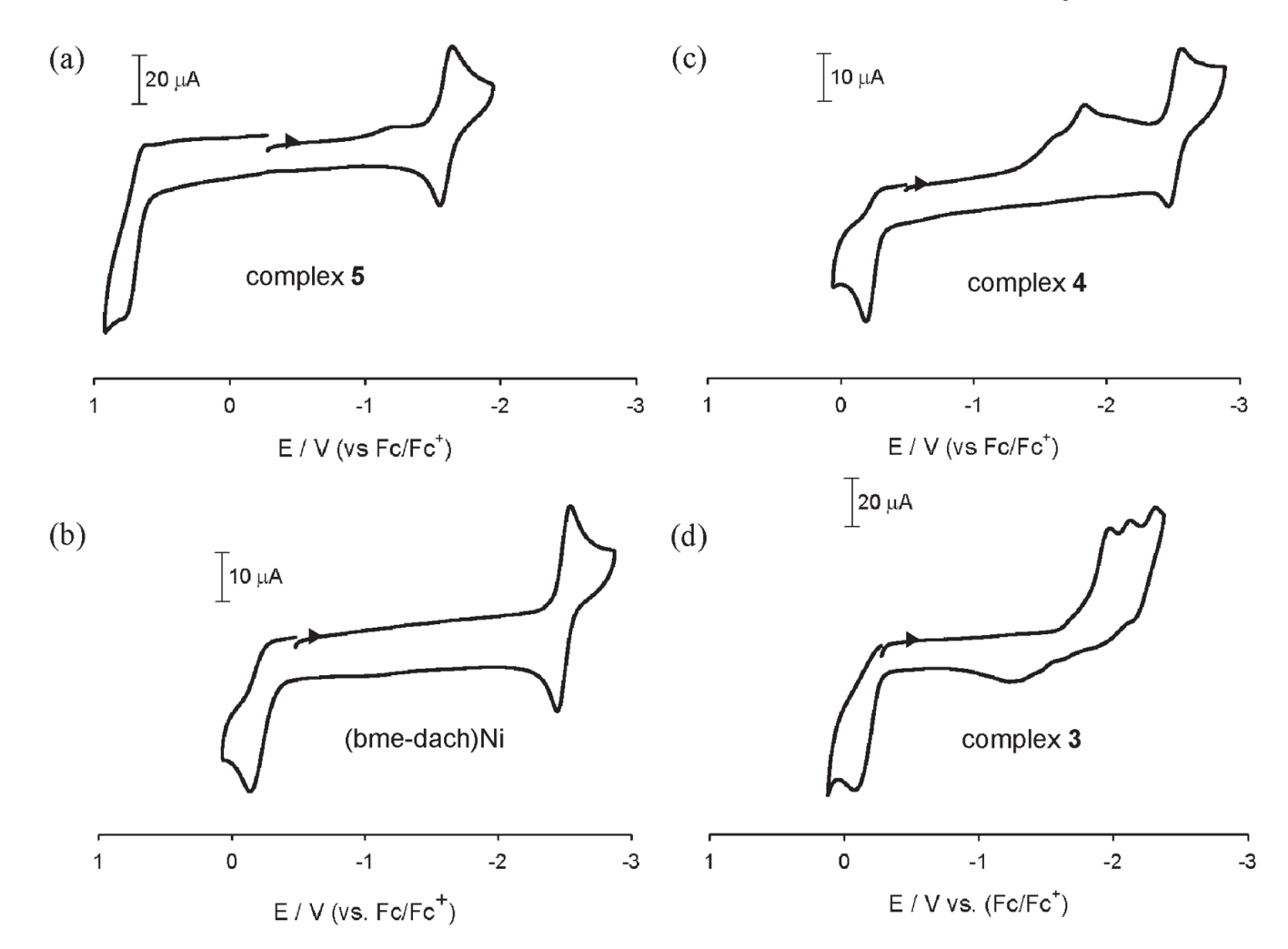


Figure 10. Cyclic voltammograms of mononuclear square planar Ni^{II} complexes in DMF and referenced to Fc/Fc^+ . (a) [(bmIme-dach)Ni](BF₄)₂, **5**; (b) (bme-dach)Ni; (c) [Ni-1'(CH₂-mIm)](Cl), **4**; (d) (mmp-mdach)Ni(Im)](Cl), **3**.

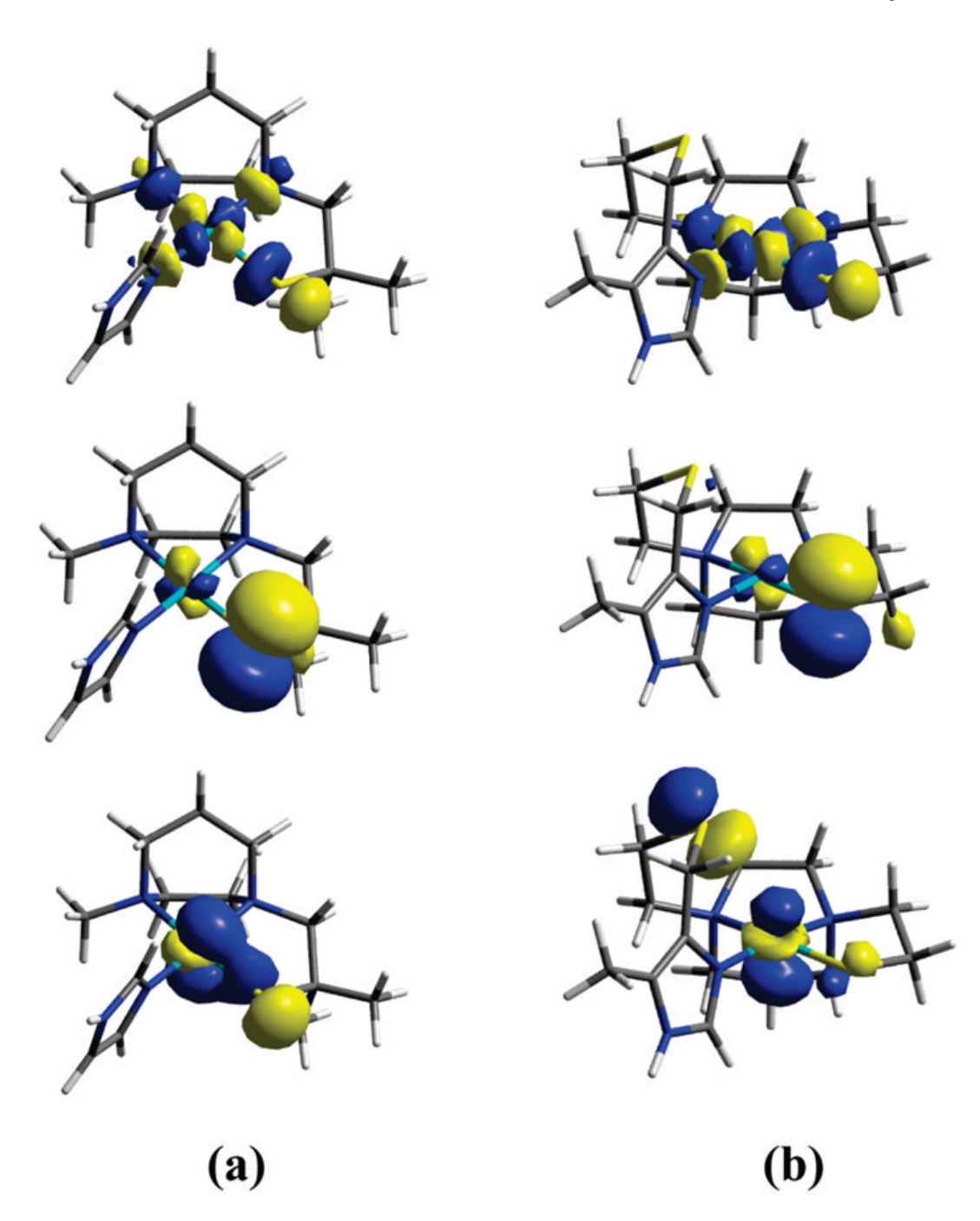


Figure 11. Frontier molecular orbitals of (a) [(mmp-mdach)Ni(Im)]Cl, 3, and (b) [Ni-1'(CH $_2$ -Im)]Cl, 4. In each column, the orbitals descend in the order LUMO, HOMO, and HOMO-1.

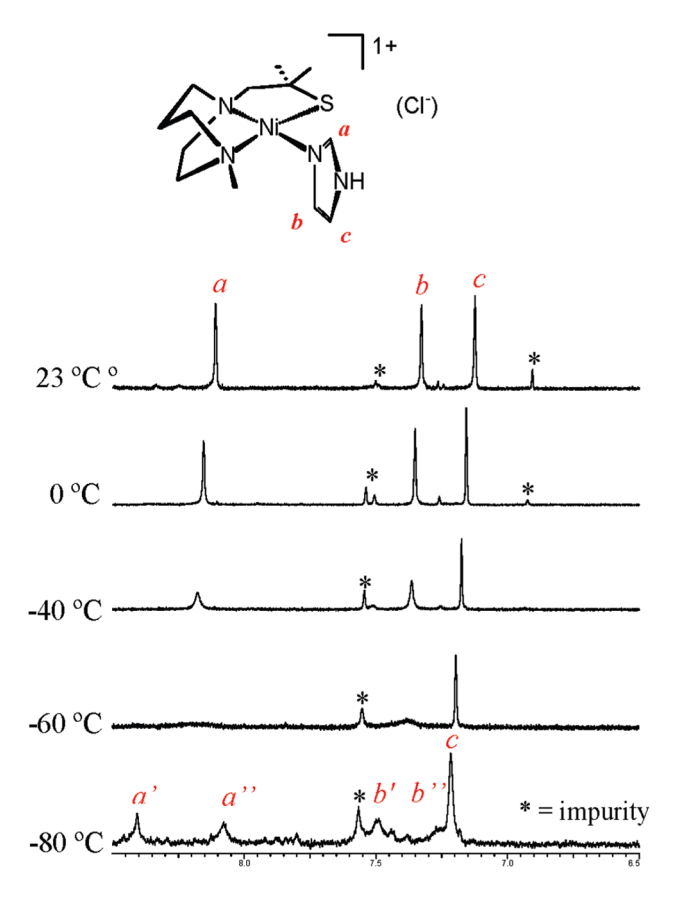


Figure 12. Variable Temperature 400-MHz ¹H NMR spectra of complex **3** in MeOH.

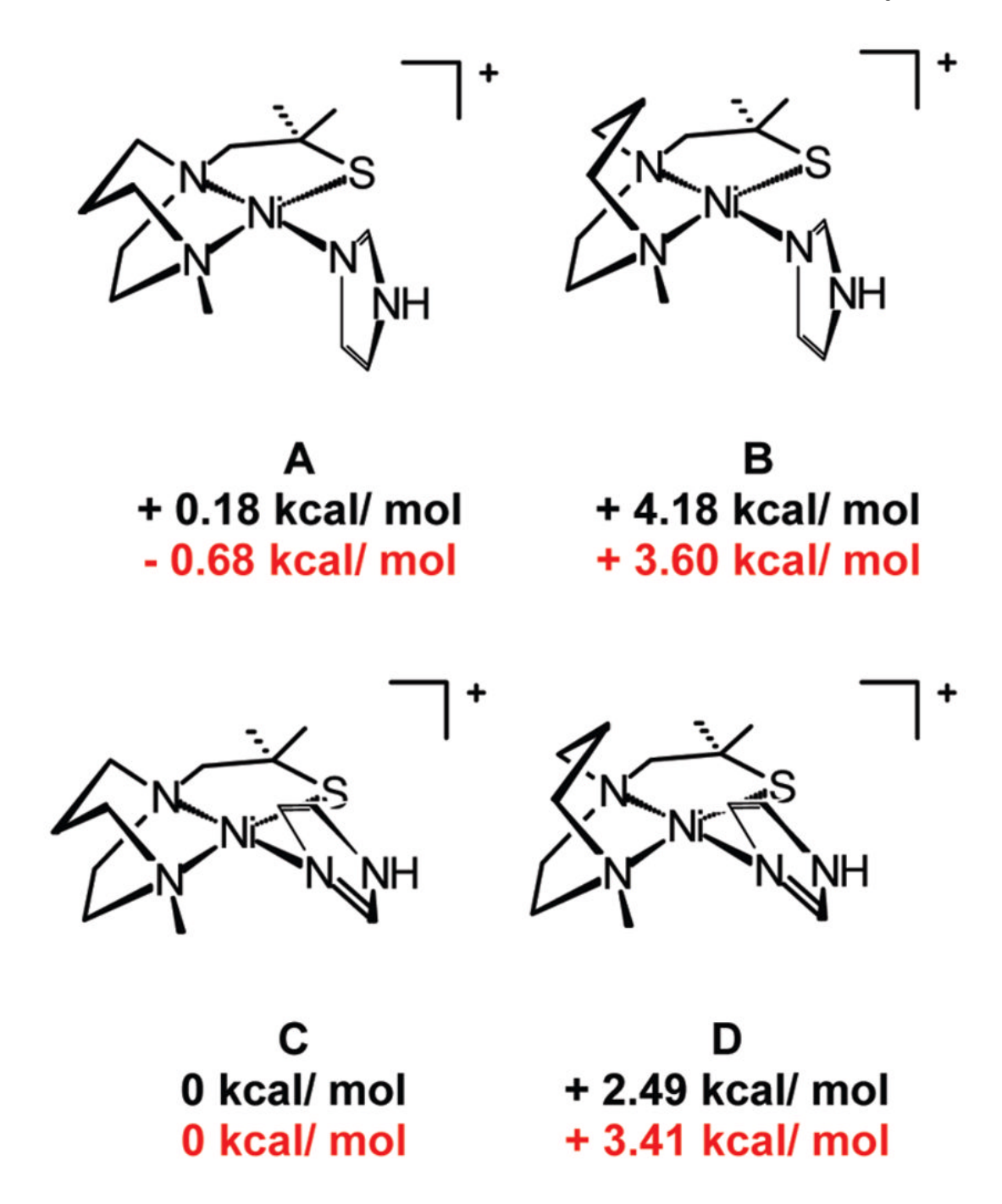
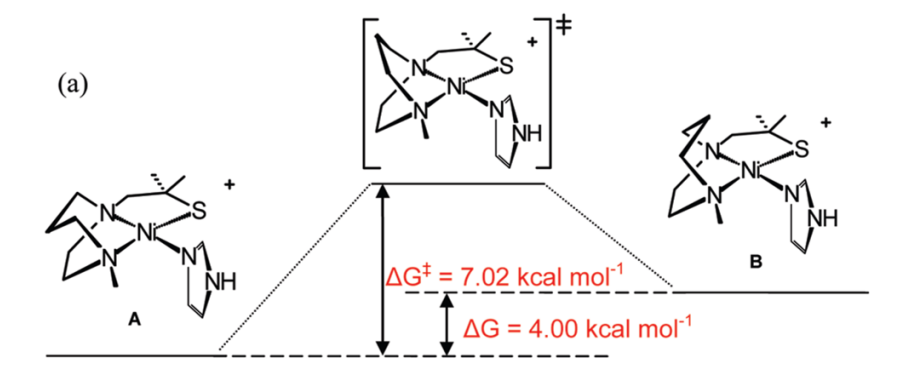
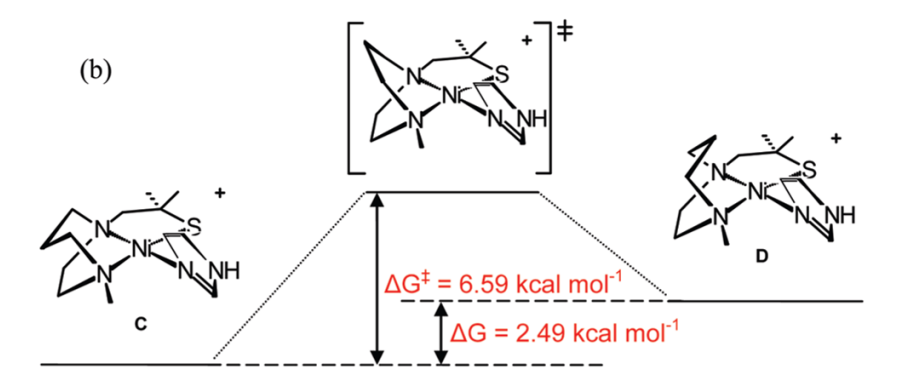


Figure 13. Four possible conformational isomers of 3 and their DFT calculated relative energies (ΔG°). Black: gas phase; red: solvent correction in MeOH.





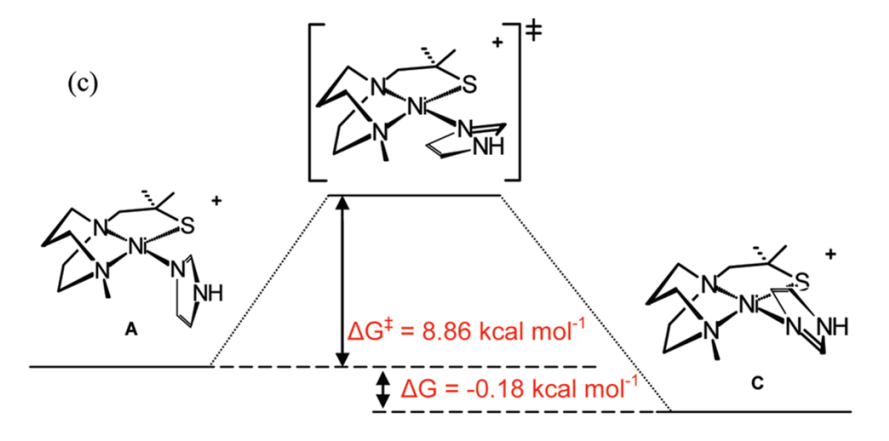


Figure 14. DFT calculated energies (kcal mol $^{-1}$): (a) Ring flip calculated with imidazole orientation same as in solid state structure; (b) Ring flip calculated with imidazole orientation 180° rotated as compared to (a); (c) imidazole rotation calculated with NiN $_2$ C $_3$ ring in chair conformation.

Figure 15. Nitroblue tetrazolium (NBT) reaction with superoxide to produce formazan.

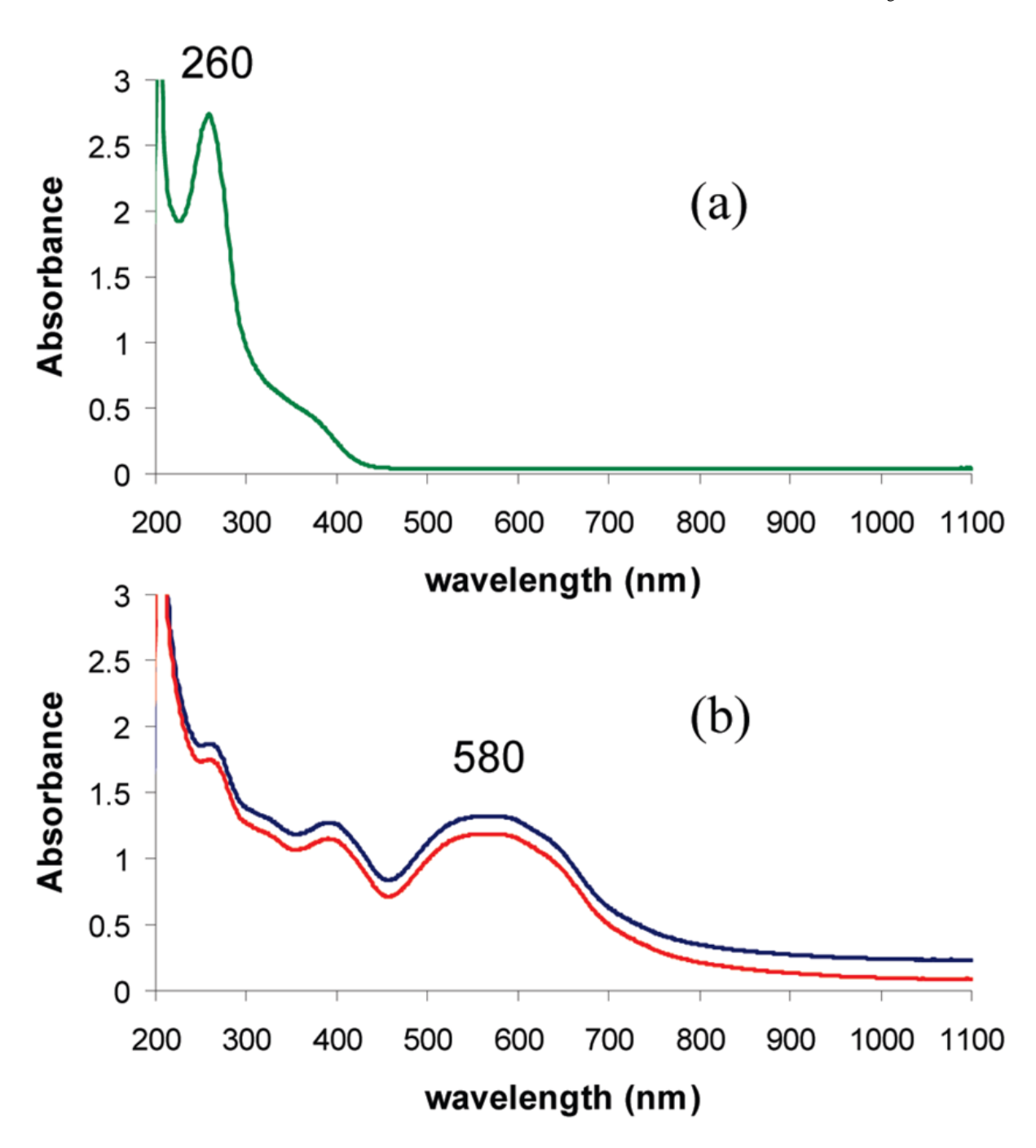


Figure 16. Electronic spectra of (a) NBT in aqueous phosphate buffer (pH7.4). (b) Blue, addition of 100 equiv of KO₂; red, 5 min after addition (formation of insoluble formazan decreases intensity).

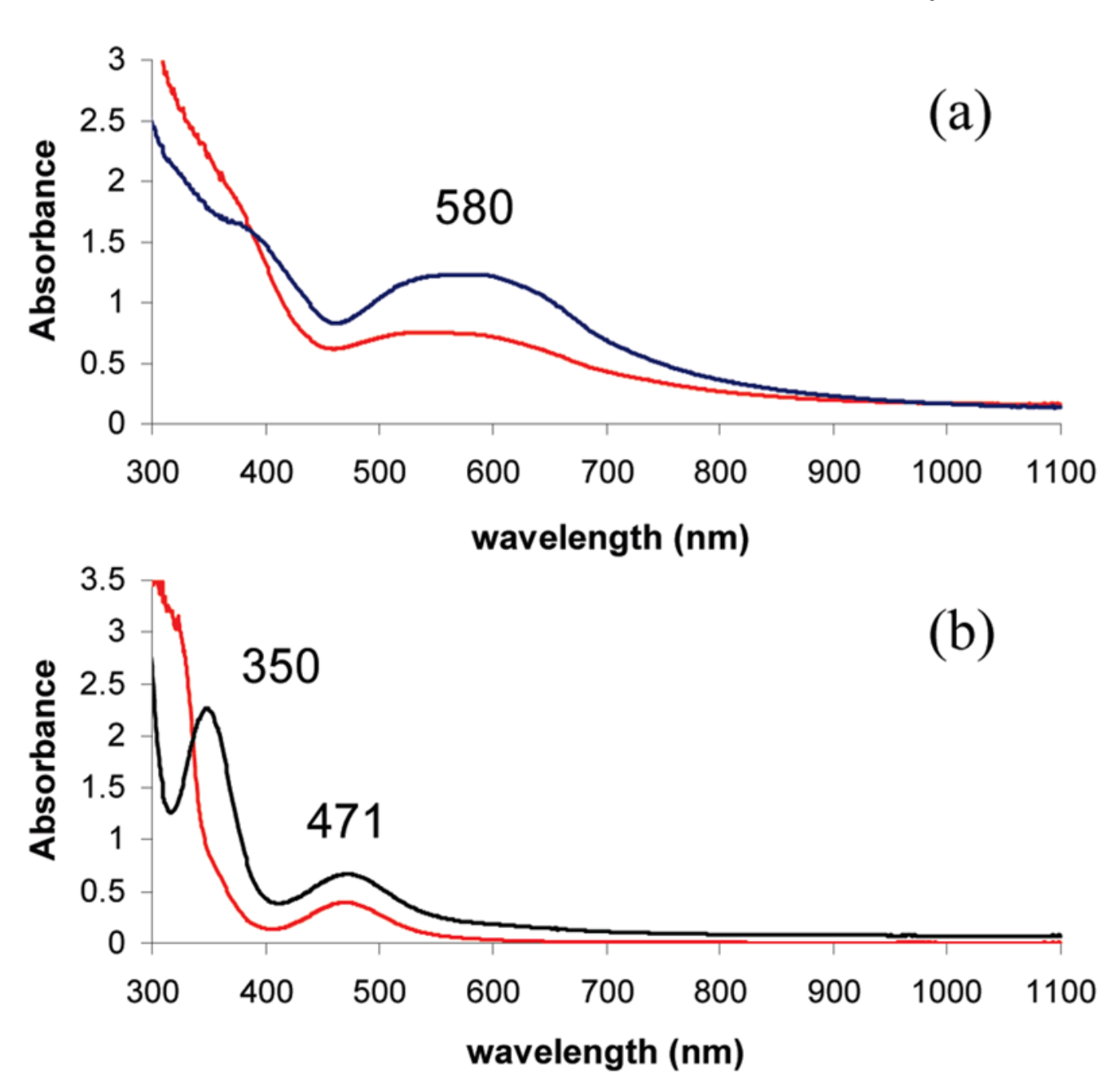


Figure 17. Electronic spectra of **3** in phosphate buffer (pH7.4). (a) Blue, addition of 100 equiv of KO_2 to NBT (61 μ M); red, addition of 100 equiv of KO_2 to NBT (61 μ M)/complex **3** (69 μ M). (b) Red, complex **3** (2.75mM); black, addition of KO_2 to Complex **3** (0.46mM)/NBT buffer solution (0.18 mM).

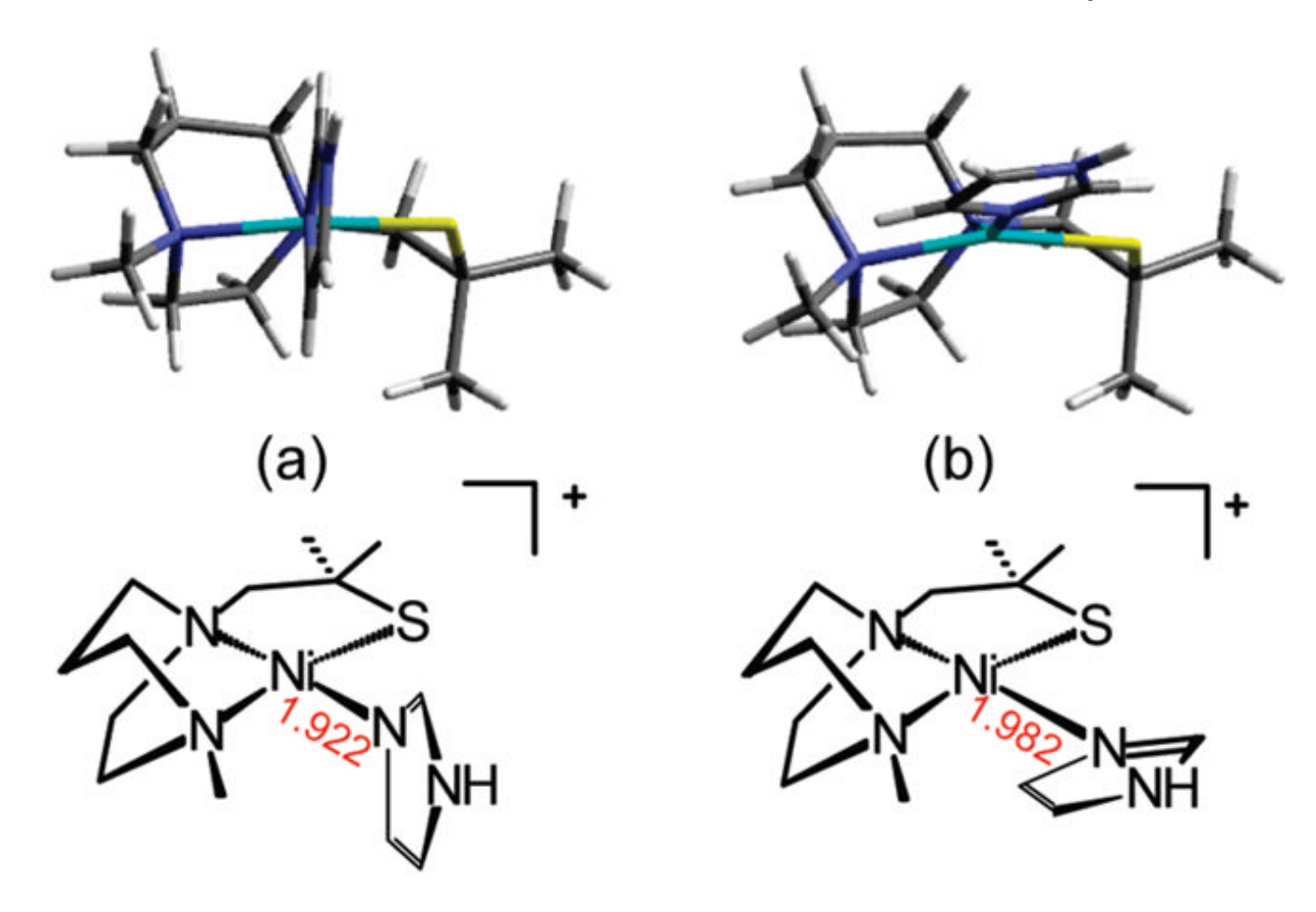


Figure 18.(a) DFT calculated ground state structure. (b) DFT calculated transition state structure.

NH + S MeCN
$$\overline{50-60 \circ C}$$
 NiX2 NaOMe MeOH $\overline{X} = (BF_4)^{-1}$ $\overline{X} = C\Gamma$

R R R \overline{B} Ni Ni S R R R \overline{B} R \overline{B}

Scheme 1.

Scheme 2.

Scheme 3.

5

Scheme 4.

Table 1

Metric Data for Complexes 1 and 2

1	2
2.069(19) Å	2.369(17) Å
2.245(16) Å	2.346(18) Å
1.923(8) Å	2.084(5) Å
1.914(8) Å	2.144(5) Å
2.837 Å	$3.268~\textrm{\AA}$
	2.331(17) Å
83.6(3)°	77.3(2)°
96.4(5)°	86.7(14)°
	92.9(14)°
	96.6(6)°
79.6(6)°	92.3(5)°
	114.6(6)°
175.4(5)°	100.6(15)°
100.5(4)°	96.8(15)°
82.1(6)°	87.8(5)°
	2.069(19) Å 2.245(16) Å 1.923(8) Å 1.914(8) Å 2.837 Å 83.6(3)° 96.4(5)° 79.6(6)°

Table 2 Molar Conductivities at 25°C

	Λ_M at $10^{-3}M~(cm^{-1}~mol^{-1}~\Omega^{-1})$		
compound	H_2O	MeCN	MeOH
[(me-mdach) ₂ Ni ₂](BF ₄) ₂ , 1	310	299	
[(me-mdach)NiCl] ₂ , 2	303	124	
$[(\text{mmp-mdach}) \text{NiCl}]_2, \textbf{2-Me}_2$	299	104	
$[(mmp\text{-}mdach)Ni(Im)](Cl), \boldsymbol{3}$	156		89
$[\text{Ni-1'}(\text{CH}_2 \cdot \text{mIm})](\text{Cl}), \textbf{4}$	164		103
[(bmIme-dach)Ni](BF ₄) ₂ , 5	223		198

Jenkins et al.

Table 3

Summary of Electronic Absorption Spectra for Complexes 1-5 and $2-Me_2{}^a$

		-VU	UV-vis: λ_{max} (nm) $(e, \text{M}^{-1} \text{ cm}^{-1})$	$(\varepsilon,\mathrm{M}^{-1}\mathrm{cm}^{-1})$		
		CT tra	CT transitions		$\mathbf{d} \to \mathbf{d} \text{ transitions}$	ansitions
[(me-mdach) ₂ Ni ₂](BF ₄) ₂ , 1^b 229 (21330) 252 (13765) 305 (13075) 354 (2503)	229 (21330)	252 (13765)	305 (13075)	354 (2503)	452 (775)	452 (775) 524 (817)
[(me-mdach)NiCl] ₂ , 2	211 (18000)	247 (17126)	307 (7816)	350 (3310)	490 (sh)	527 (967)
$[(mmp-mdach)NiCI]_2$, 2-Me ₂	205 (24575)	244 (21298)	283 (11940)	326 (6115)	426 (988)	532 (904)
(mmp-mdach)Ni(Im)](Cl), 3	211 (21460)			288 (10767)	340 (sh)	467 (501)
$[Ni-1'(CH_2-mIm)](CI)$, 4	211 (16980)			288 (6052)		469 (235)
[(bmIme-dach)Ni](BF $_4$)2, 5		233 (2232)		280 (sh)		449 (29)

 $^{\mathcal{Q}}$ Unless specified otherwise, all results were obtained from MeOH solutions.

b

The electronic spectrum of [(me-mdach)2Ni2](BF4)2 was measured in MeCN.

Page 41

Table 4

Electrochemical Data for Complexes 1–5^a

	$E_{\text{ox}}(V)$	$E_{\rm red}\left(\mathbf{V}\right)$	
complex	E_{pa}	$E_{1/2}$	$E_{ m pc}$
$[(\text{me-mdach})\text{Ni}]_2(\text{BF}_4)_2, 1$	+0.14	-1.30	-2.02
[(me-mdach)NiCl] ₂ , 2	+0.06	-1.45	-2.03
$[(mmp\text{-}mdach)NiCl]_2, \textbf{2-}Me_{\textbf{2}}$	+0.04	-1.58	-1.91
$(mmp\text{-}mdach)Ni(Im)](Cl), \boldsymbol{3}$	-0.07		-1.96
			-2.13
			-2.31
$[\text{Ni-1'}(\text{CH}_2\text{-mIm})](\text{Cl}),\boldsymbol{4}$	-0.18	-2.50	-1.82
[(bmIme-dach)Ni](BF $_4$) $_2$, 5	+0.77	-1.59	-1.21
(bme-dach)Ni	-0.14	-2.50	

 $^{^{}a}$ Ar deaerated DMF solution (0.1 M n Bu4NBF4). All experiments were recorded using a glassy carbon working electrode (A=0.071 cm 2) referenced to Fc/Fc $^{+}$ and a Pt counter electrode at a scan rate of 200 mV/s.